



Abschlussarbeit im Bachelorstudiengang Physik

Characterization of the TRISTAN Silicon Drift Detectors with Krypton Conversion Electrons

Untersuchung der TRISTAN Silizium Drift Detektoren mit Krypton
Konversionselektronen

Xavier Pawlowski

14. September 2018

Max-Planck-Institut für Physik

Erstgutachter (Themensteller): Prof. Dr. Susanne Mertens
Zweitgutachter: Prof. Dr. Laura Fabbietti

Contents

Introduction	v
1 Neutrinos and the KATRIN/TRISTAN Experiment	1
1.1 KATRIN and the neutrino mass	1
1.1.1 Components of KATRIN	3
1.2 Sterile neutrinos in KATRIN	4
1.2.1 Signature of sterile neutrinos in beta decay	5
1.2.2 TRISTAN project	5
2 TRISTAN prototype setup	7
2.1 Silicon Drift Detector: Fundamentals	7
2.2 7-pixel prototype detector	9
2.3 Experimental setup	10
2.3.1 Design of detector holding structure	11
2.4 Optimization of DAQ settings	13
2.4.1 Determination of the optimal peaking time	13
2.4.2 Determination of the optimal threshold value	15
3 Krypton measurement	17
3.1 Dead-layer determination with Kr-83m	17
3.2 Empirical model for electron & photon peaks	21
3.2.1 Photon response	21
3.2.2 Electron response	23
3.3 Energy calibration	25
3.4 General performance	27
3.4.1 Energy resolution	27
3.4.2 Pixel homogeneity	30
3.5 Determination of the dead-layer thickness	32
3.5.1 General idea	32
3.5.2 Observed shift of electron peak position	33
3.5.3 Comparison to theoretical model	36
4 Conclusion & outlook	39

Contents

A Appendix	41
A.1 Second chapter appendix	41
A.2 Third chapter appendix	42
Bibliography	45

Introduction

Numerous observations point out a deficiency of matter in the universe of approximately 80% [1, 2]. To explain this shortcoming, called 'dark matter', many hypotheses have been proposed. A promising candidate for a dark matter particle would be a keV-range sterile neutrino, since it constitutes a minimal extension of the standard model. A unique way to investigate sterile neutrinos in a laboratory environment is given through the tritium β -decay. Pushing the limits of technology, the **K**Arlsruhe **T**RItium Neutrino experiment (KATRIN) collaboration has developed a setup in order to measure the electron anti-neutrino's mass using a high luminosity tritium source. The TRISTAN project (**T**Ritium **I**nteraction on **S**terile to **A**ctive Neutrino mixing) aims to search for a keV-range sterile neutrino benefiting of KATRIN's outstanding setup. For this purpose, some features of KATRIN need to be upgraded, mainly the detector and read-out system. (The current detector is not suited for a sterile neutrino search, as much higher count rates are required compared to the currently performed electron anti-neutrino mass measurement.) Because of the different demands, a silicon drift detector is an appropriate choice for the new detector design. In order to see the imprints of the sterile neutrino in the spectrum, the energy of the electrons originating from the β -decay has to be known with great precision. A high energy resolution and a low detection threshold are crucial requirements that can only be assured if the detector presents a thin dead-layer, since it affects the energy of incoming electrons. The dead-layer is an undesired but unavoidable feature of silicon drift detectors and one should therefore aim to reduce it to its absolute minimum.

In this work, an investigation of the dead-layer of a TRISTAN Prototype Silicon Drift Detector was performed. A source of $^{83\text{m}}\text{Kr}$ was used, as it emits quasi-monoenergetic photons and electrons. Unlike the electron peaks, the photon peak position is not affected by the dead-layer. Electrons, on the other hand, always deposit a fraction of their energy in the dead-layer while crossing it. For this reason, photons can be employed in order to calibrate the energy scale, while the shift of the electron peak positions with respect to their theoretical line is an indicator of the dead-layer thickness.

The investigated 7-pixel detector chip was produced at the Halbleiterlabor of the Max Planck Society. The characterization took place in a specifically designed vacuum test setup. For the final result, a simple calculation allowed for an estimation of the actual dead-layer thickness.

First, a brief introduction to the KATRIN experiment will be given in chapter 1. In the following chapter 2, the studied TRISTAN prototype detector will be presented. Chapter 3 describes the undertaken procedure to determine the dead-layer thickness.

1

Neutrinos and the KATRIN/TRISTAN Experiment

In this chapter a brief introduction to the KATRIN Experiment will be given together with a short description of its main components. In section 1.2 the imprint of a sterile neutrino in the β -decay of tritium will be explained. Finally, in section 1.2.2 the TRISTAN project will be presented.

1.1 KATRIN and the neutrino mass

The **K**arlsruhe **T**ritium **N**eutrino experiment (KATRIN) is a large-scale tritium beta decay experiment to directly measure the effective mass of the neutrino.

KATRIN unites the efforts of many research groups from Germany, the United Kingdom, Russia, Czech Republic and the United States. In June 2018 KATRIN took the first tritium data. This successful first measurement campaign demonstrates the stability and functionality of the entire beamline.

The neutrino mass manifests itself as a distortion of the tritium beta decay spectrum close to its endpoint. If one assumes that the neutrino does carry a non-zero mass, the electrons participating in the β -decay process will never reach an energy equal to the endpoint energy. Their maximal attainable energy will be equal to the one presented in equation 1.1, as some of the released decay energy will have to be used for the creation of the electron anti-neutrino.

$$E_{e,\max} = E_{\text{endpoint}} - m_\nu c^2 \quad (1.1)$$

Knowing the endpoint energy to be equal to the mass difference between the parent and daughter nuclides ($E_{\text{endpoint}} = 18.6 \text{ keV}$), the neutrino mass can be determined by analyzing the energy distribution of the electrons close to the 18.6 keV mark. Figure 1.1 shows the expected energy spectrum for a neutrino mass of 1 eV compared to 0 and 0.3 eV. The energy distribution presents different shapes and the endpoint energy is shifted away from the 18.6 keV mark for a non-zero neutrino mass. For a vanishing neutrino mass, the endpoint shape presents an exponential-like decline,

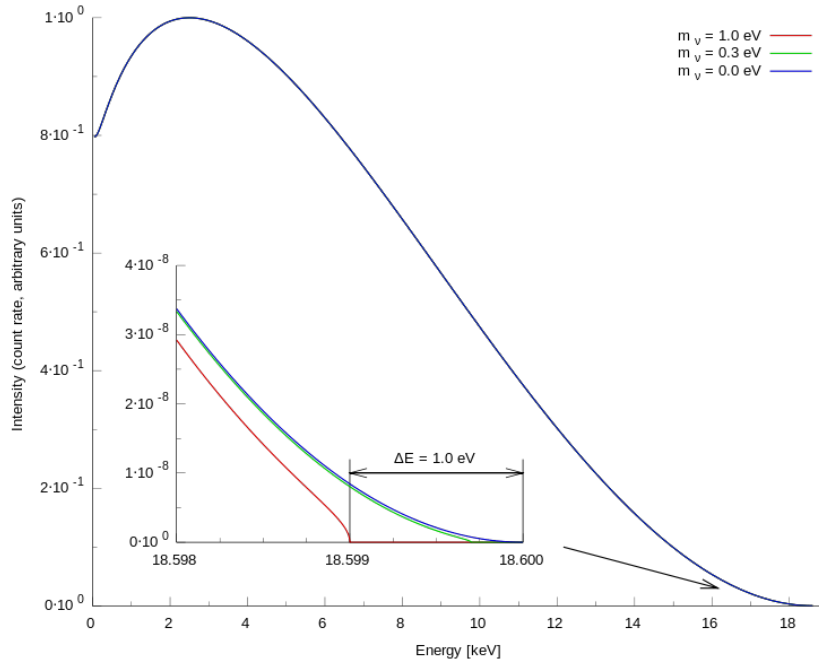


Figure 1.1: Expected energy spectrum of the tritium beta decay assuming a neutrino mass of $m_\nu=0\text{ eV}$ (blue line), $m_\nu=0.3\text{ eV}$ (green line) and $m_\nu=1\text{ eV}$ (red line). A clear difference in the shape of the curve as well as a different endpoint energy can be observed for the three different neutrino mass assumptions. [3]

while for a non-zero mass, the electron energy spectrum ends in a much more abrupt fashion.

Tritium has a half life of approximately 12.3 years. Its endpoint energy of 18.6 keV is particularly low compared to other potential sources. Because of these properties it is a suiting candidate for the neutrino mass measurement.

As KATRIN only analyzes the very end of the electron energy spectrum, the low endpoint energy is beneficial for the measurement since there are relatively many events in the analyzed energy range. If one chose a source with a higher endpoint energy, it would need to have a higher activity. This is due to the fact that more decays would be needed in order to have enough events in the last few eV of the β -electrons energy spectrum. As the whole energy spectrum is squeezed into 18.6 keV in case of tritium, the imprint of the neutrino mass is relatively bigger than it would be for sources with higher endpoint energies. Another consequence of tritium's properties is that the required quantity of tritium is relatively low compared to other potential sources.

Moreover, the electron shell configurations of Tritium and its daughter nucleus

${}^3\text{He}^+$ are very simple, which renders the calculations of various corrections (e.g. due to interaction of the β -electron with the tritium source) simple. [4, 5]



The KATRIN experiment is expected to reach a sensitivity of $0.2 \text{ eV}/c^2$ after 3 years of data collection. After this time the statistical and systematic uncertainties will contribute equally to the collected data. If KATRIN does record a positive signal pointing to a non-zero neutrino mass, its discovery potential would be of 5σ (3σ) for a neutrino mass of $m_\nu = 0.35 \text{ eV}/c^2$ ($0.3 \text{ eV}/c^2$). In the event of no positive signal being picked up, a new upper limit for the mass of the electron neutrino will be set equal to $m_\nu < 0.2 \text{ eV}/c^2$ with a 90% confidence level. [4]

So far the upper limit set by direct neutrino mass measurements has been established by the Mainz Neutrino Mass Experiment and the Troitsk ν -mass Experiment yielding a result of $m_\nu < 2.3 \text{ eV}/c^2$ with a 95% confidence level. [6, 7]

1.1.1 Components of KATRIN

To reach the sensitivity mentioned in section 1.1, a complex experimental setup is unavoidable. Figure 1.2 [8] presents an overview of the whole KATRIN setup. In the following, the main components are introduced.

Windowless Gaseous Tritium Source (WGTS)

The tritium is being provided in its gaseous form using a **Windowless Gaseous Tritium Source** (WGTS). It assures the required stable, high luminosity flow of beta-electrons. To keep the uncertainties of the recorded data at its lowest, among other factors, the source's activity has to be known with an extremely high precision. To monitor the number of decays, the column density of the tritium gas $\rho = 5 \cdot 10^{17} \text{ molecules}/\text{cm}^2$ cannot present any major fluctuations. The variation in tritium density has to be controlled at all times and has to be known with a precision of 0.1%. This can only be attained by an absolute control of the temperature and rate at which the tritium gas is being injected. In order to achieve this, a liquid neon cooling system has been installed which can assure a stability of $\pm 30 \text{ mK}$. The injection rate is being controlled by turbomolecular pumping sections and achieves likewise a stability of 0.1%. [4, 9]

Spectrometer

In order to filter out the electrons that are not in the energy region of interest, a high resolution spectrometer, called MAC-E Filter (**M**agnetic **A**diabatic **C**ollimation combined with an **E**lectrostatic Filter), is used. Two superconducting solenoids

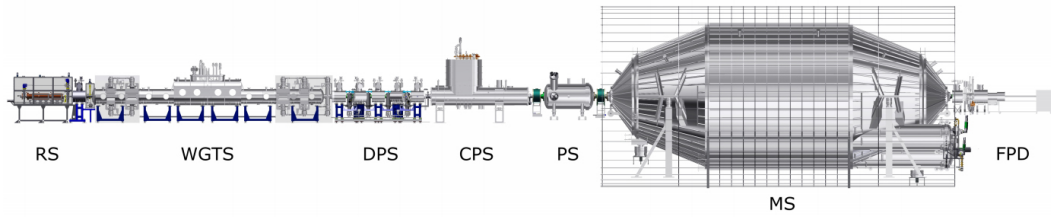


Figure 1.2: "Schematic overview of the 70 m KATRIN beamline: (RS) rear section, (WGTS) windowless gaseous tritium source, (DPS) differential-pumping section, (CPS) cryogenic pumping section, (PS) pre-spectrometer, (MS) main spectrometer, and (FPD) focal-plane detector." [8]

produce a strong magnetic field that adiabatically guides the electrons through the spectrometer. The magnetic field slowly varies in space, being the strongest at the entrance and at the exit window and presenting a minimum in the middle of the filter. In the center of the spectrometer, where the magnetic field is the lowest, the electrons face an electric potential, which presents a high-pass filter. The electrons that have enough energy to surpass it are then re-accelerated in the second half of the structure and collimated onto the detector. Electrons that do not have enough energy to pass the filter get reflected. The spectrometer's resolution is determined by the ratio of the maximal (edges) and minimal (middle) magnetic field. [4, 10]

Focal plane detector

The KATRIN detector itself is made of an 148 pixel p-i-n diode array and detects the low energy electrons that manage to pass the spectrometer. As the flux of β -electrons from the spectrometer is not completely focused, the detector needs to cover an area of approximately 63 cm^2 . Since the detector performs an integral measurement, its requirements are not as high as they are in the case of detectors carrying out a differential measurement. [11] During an integral measurement all electrons above a certain energy threshold are being counted, while a differential measurement registers the energy of each electron.

1.2 Sterile neutrinos in KATRIN

In a minimal extension of the Standard Model (SM), a new particle, namely a fourth, sterile, neutrino, is being proposed [2, 12]. While the active neutrinos interact via the weak interaction and gravity, the *sterile* neutrino would only interact via gravity. Having right handed chirality, it would complement the active neutrinos that were observed to all be left handed. Like a counterbalance, it would also present a

much higher mass than the active neutrinos (models predict sterile neutrino masses in ranges varying from eV, to 10^{15} GeV). Light sterile neutrinos in the eV-range are predicted from observed reactor anomalies, while the possibly important mass of GeV-sterile neutrinos is motivated by the *Seesaw mechanism* referencing the particularly low mass of the active neutrinos. A notable DM candidate would be a sterile neutrino with a mass in the keV-range, since it would fall in the category of **Warm Dark Matter** (WDM). The WDM theory can explain the tensions in simple astronomical models [2, 13, 14].

1.2.1 Signature of sterile neutrinos in beta decay

It is assumed that the sterile neutrino does participate in the oscillation of active neutrino eigenstates. The existence of a possible keV-range sterile neutrino would be able to influence the β -decay energy spectrum at any point, depending only on its actual mass. The magnitude of the impact is determined by the mixing probability between the active and the sterile neutrino eigenstates. [15, 16]

The β -electrons carry away an energy equal to the endpoint energy minus the energy of the neutrino. The minimal energy that can be carried away by the sterile neutrino is equal to $E_{\text{sterile,min}} = m_{\text{sterile}}/c^2$. Due to the mixing between active and sterile neutrino states, two regions can then be distinguished in the tritium decay spectrum. If the electron carries away more energy than $E_{\text{endpoint}} - m_{\text{sterile}}$, the tritium decay into the keV-range sterile neutrino is not allowed, as there is not enough decay energy left for its creation. If, on the other hand, the electron carries away less energy during the decay process, the sterile neutrino can be created. The unification of both regions results in a kink in the electron energy spectrum which can be seen in figure 1.3. The effect is relatively big in said figure due to a largely exaggerated mixing angle [16]. In order to be detectable in the tritium spectrum, the sterile neutrino mass needs to be at least a few keV below the endpoint energy of 18.6 keV [17].

1.2.2 TRISTAN project

As stated in section 1.1.1, the infrastructure developed in Karlsruhe for the KATRIN experiment presents some outstanding performances. The goal of the TRISTAN project (**TR**itium **I**nteraction on **S**terile to **A**ctive **N**eutrino mixing) is to make use of the luminosity of the WGTS as well as the high resolution of KATRIN's spectrometer in order to search for the kink-like signature of the sterile neutrino. Since the sterile neutrino mass is unknown, the kink may appear at any energy-range. Therefore, TRISTAN will need to analyze the whole tritium spectrum, which requires an upgrade of some of the setup's components.

The electronic potential in the spectrometer will be lowered so that electrons of

all energies can reach the detector. To attain the required statistics of 10^{16} electrons within three years of data taking, the detector and read-out system need to be upgraded in order to handle the higher count rates. A prototype for the novel detector system is being presented in the following chapter (2).

With no retarding potential limiting the flux of electrons to the detector, the rate would be in the order of $\approx 10^{10}$ counts per second. Since the requirements for a detector to handle the such a high rate would be too important, the luminosity of the WGTS will have to be reduced so that a rate of $\approx 10^8$ counts per second is reached.

The TRISTAN project is expected to upgrade KATRIN for the sterile neutrino search in approximately five years from now when KATRIN's neutrino mass program has finished.

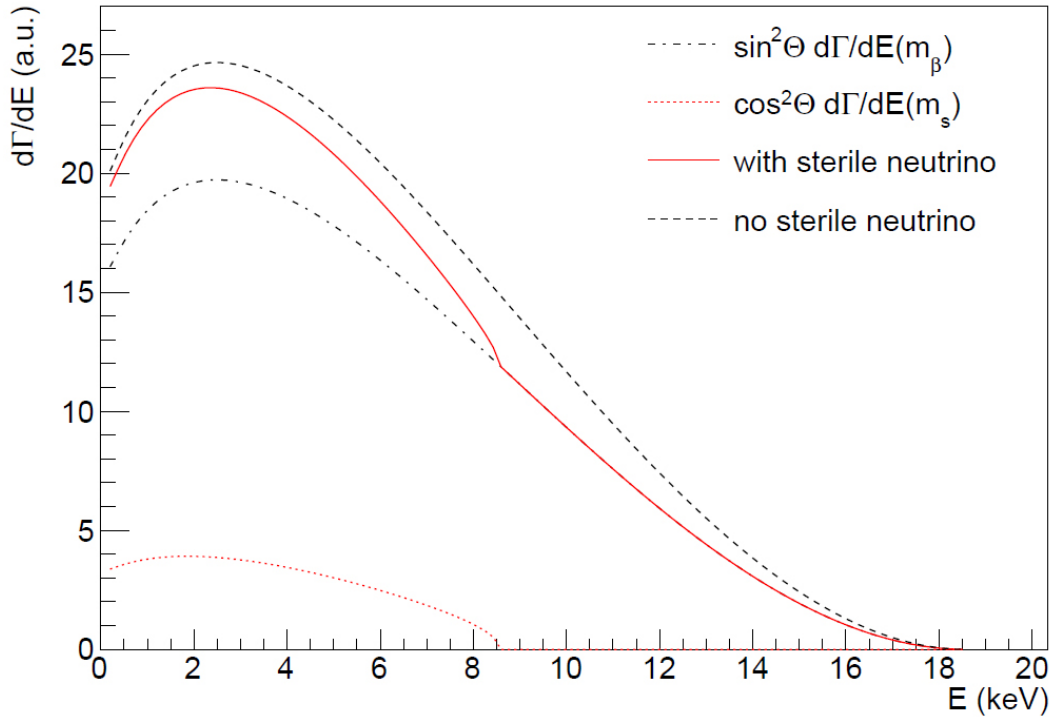


Figure 1.3: [18] Tritium β -decay energy spectrum. The outer dashed line represents the spectrum with no mixing between active and sterile neutrino states, while the solid red line shows the spectrum with a $m_{\text{sterile}} = 10$ keV sterile neutrino mixing assuming a mixing angle of $\sin^2\theta^2 = 0.2$. The mixing angle being largely exaggerated, the kink-like feature is clearly visible at an energy $E = E_{\text{endpoint}} - m_{\text{sterile}}$ [16].

2

TRISTAN prototype setup

Since TRISTAN will save the whole β -decay spectrum produced by the tritium source, one of the biggest challenges will be the handling of the much higher count rates compared to KATRIN. The KATRIN detectors have to deal with approximately 1 count per minute. For TRISTAN to reach the needed statistics of 10^{16} electrons within three years of data collection, the upgraded setup will have to handle count rates in the order of 10^8 counts per second [15, 19]. It should be noted that this rate will be then distributed onto multiple detectors which will then have to manage rates in the order of 10^5 counts per second [15]. Let alone this requirement calls for the design of a new detector and data acquisition system. The employed detectors also demand an exceptional energy resolution of the incoming electrons, since the effect of the sterile neutrino on the tritium spectrum is expected to be very small. Further, the bigger the detector's size, the smaller the undesired effect of charge sharing 3.4.1 between different pixels. The best choice to fulfill these prerequisites lead to a **Silicon Drift Detector (SDD)** with ≈ 3500 pixels. [15]

In the following chapter a brief introduction to SDDs will be given in section 2.1. Furthermore, the investigated TRISTAN prototype detector as well as the experimental setup will be described in sections 2.2 and 2.3 respectively. In order to minimize the uncertainties of the recorded data, the basic settings of the **Data AcQuisition (DAQ)** system were optimized. The obtained parameters are being presented in section 2.4.

2.1 Silicon Drift Detector: Fundamentals

As already specified, silicon drift detectors are a very popular choice in order to detect x-rays and electrons at high count rates. One of their characteristics is a very small anode. Being proportional to the anode's size, the capacitance of silicon drift detectors is also small. This is an important requirement for the handling of high count rates, since it keeps the noise low at short shaping times. For a more detailed explanation of the influence of shaping time on the signal please refer to section 2.4.1.

Silicon, being a semiconductor, possesses a direct band gap of $E_{\text{gap}} = 3.6$ eV. Yet, the energy required for the creation of an electron-hole pair E_{pair} is slightly higher

than the band gap energy, $E_{\text{pair}} \approx 3.64 \text{ eV}$ [20]. An ionizing particle with an energy higher than E_{pair} can interact with a valence-band electron in the silicon and excite it into the conduction band, creating an electron-hole pair. The amount of charge carriers produced depends on the energy of the incoming particle. If the particle deposits its energy in the active region of the SDD, the generated charge carriers are guided by an electric field created inside the detector. The electric field is produced by the p+doped drift rings surrounding the anode. The negative charge carriers are led towards the anode where they leave the bulk semiconductor due to the applied bias voltage. A sketch of the main features of a silicon drift detector can be seen in figure 2.1. [21–23]

An undesired but inevitable feature of SDDs is the presence of a dead-layer that all particles have to pass in order to be detected. The ionization produced in the dead-layer will not (or only partly) be registered by the detector, since the internal electric field is unable to collect the charge carriers generated near the detector's borders. Therefore, the need to reduce the dead-layer thickness to its absolute minimum is crucial for a precise measurement, else the electrons' energies cannot be determined accurately.

Other factors restraining the resolution of silicon drift detectors include the Fano limit and the electronic noise. While one can try to reduce the electronic noise (see section 2.4.1), the Fano limit cannot be surpassed. It describes the statistical fluctuations in the charge generation process. The Fano factor F is defined as the quadratic deviation of the number of generated charge carriers divided by the average number of generated charge carriers (eq.2.1) [24].

$$F = \frac{\langle n^2 \rangle - \langle n \rangle^2}{\langle n \rangle} \quad (2.1)$$

The Fano factor depends on the energy E_0 of the ionizing particle and also presents a slight temperature dependence. But since the variation of the Fano factor in the considered energy range is below 2% and the temperature was stable during the measurement, the constant value of $F = 0.124$ was adopted [20]. Assuming that incoming monoenergetic particles create a peak of a Gaussian shape in the spectrum, the variance σ^2 of the peak consists of the sum of the Fano variance (eq.2.2) and the variance of the electronic noise (eq.2.3) with n_{ENC} being the dimensionless equivalent noise charge, which describes the peak broadening due to electronic noise [24].

$$\sigma_{\text{Fano}}^2 = F \cdot E_{\text{pair}} \cdot E_0 \quad (2.2)$$

$$\sigma_{\text{noise}}^2 = E_{\text{pair}}^2 \cdot n_{\text{ENC}}^2 \quad (2.3)$$

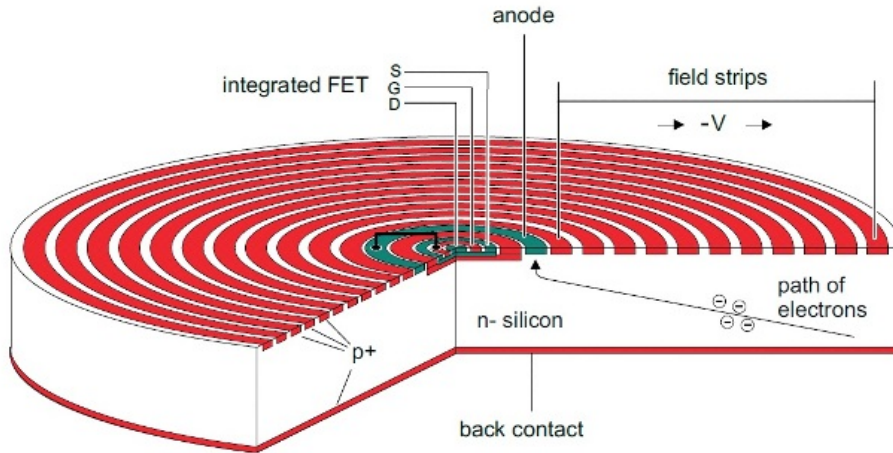


Figure 2.1: Illustration of the basic components of a silicon drift detector [21]

2.2 7-pixel prototype detector

The investigated TRISTAN prototype silicon drift detector shown in figure 2.2 [19] consists of 7 hexagonal pixels of 2 mm diameter and $450\ \mu\text{m}$ thickness. The detector was fabricated by the **H**alb**L**eiter**L**abor (HLL) of the Max Planck Society [25]. Due to their hexagonal shape, the separate pixels can form an array that does not display any gap between the pixels eliminating the dead area of the detector. Having a size of $90\ \mu\text{m}$ only, each pixel's anode has a likewise small capacitance of roughly 110 fF necessary for a good noise performance and allowing the use of very short shaping times 2.4.1. The detector has been equipped with the readout **C**UBE **A**pplication-**S**pecific **I**ntegrated **C**ircuit (ASIC) from the Italian company XGLab [26]. The CUBE includes a **F**ield **E**ffect **T**ransistor (FET) and presents the first signal amplification stage. Its noise performance matches the efficiency of SDDs with integrated FETs. [15, 19]

The produced detector possesses all the requirements mentioned in the previous section, namely the capability to handle high count rates as well as a relatively good energy resolution. For the final TRISTAN project, an energy resolution amounting to 300 eV at 30 keV for electron [18] as well as the capability to handle count rates in the order of 10^5 counts per second per pixel [15] are required. The requirement linked to the rate calls for a minimum number of 1000 pixels in the final array. For budgetary reasons as well as to assure good readout electronics, the final number of pixels should not be much higher. The current design consists of an array of 3500 pixels [19].

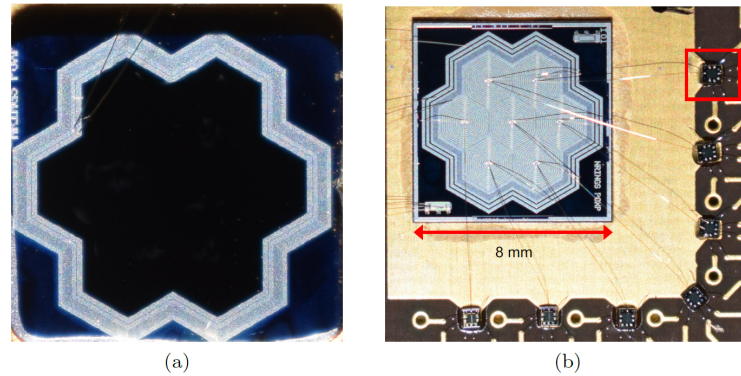


Figure 2.2: Photographs of (a) entrance window and (b) the backside of the a TRISTAN prototype detector. The individual anodes of the separate pixels are connected to their individual CUBE preamplifiers (one circled in red) [19]. Note: this is not the investigated detector, but it presents the same design.

2.3 Experimental setup

The block chain of the experimental setup can be seen in figure 2.3. The 7-pixel detector itself is being attached to a **Printed Circuit Board (PCB)**. To attain the best possible energy resolution, the acquired signal has to be amplified as soon as possible. In this way, the contribution of the electronic noise is being limited. For this reason, the PCB already includes a first amplification step. In fact, the signal from each pixel is being directly magnified with a CUBE pre-amplifier. The CUBEs are connected to the pixels via thin bonds in order to minimize the capacitance and further reduce electronic noise. After the pre-amplification, normal electronic connections can be used.

After being amplified by the CUBE, the signal is still too weak to be converted into a digital form. The main amplification stage takes place on the bias board. From there it is being fed to the **DANTE Digital Pulse Processor (DPP)**. The DPP has also been provided by the XGLab company. It converts the analog voltage signal to a digital one that can then be registered on a computer. Since both the detector and the bias board need to be alimented with low and high voltage, two voltage sources of approximately 10 and 230 V have to be supplied. The voltages are being fed to the PCB through the bias board supplying the detector's drift rings and CUBE pre-amplifiers with the high and low voltage respectively [17]. The bias board also performs collective resets of all pixels so that they remain synchronized.

As one of the main goals of this work is to analyze the detector response function for electrons, the detector and the source had to be placed inside a vacuum chamber. Otherwise, the electrons emitted from the source would be unable to reach the

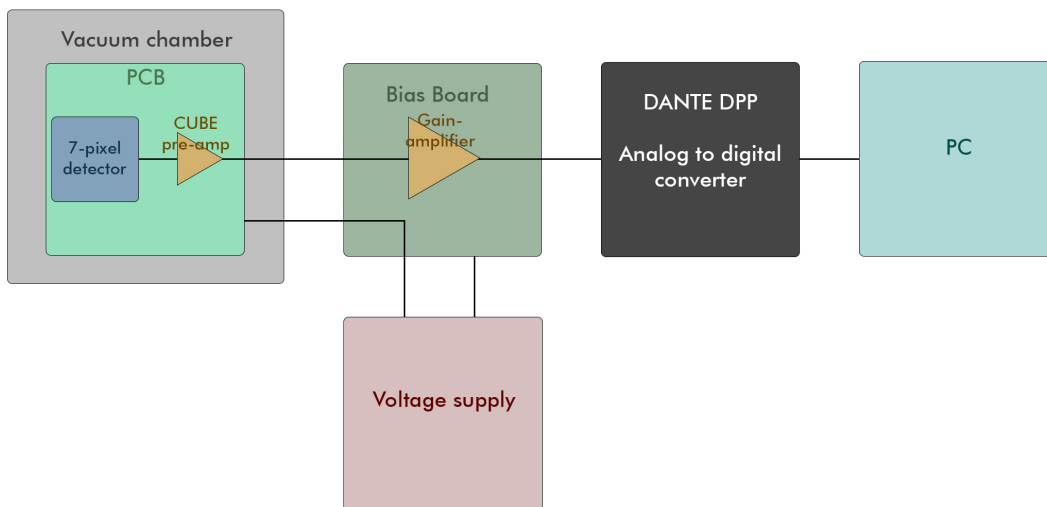


Figure 2.3: Chain of the basic components of the experimental setup. The signal registered by the detector passes a first amplification step while being still inside the vacuum chamber. However, the main amplification takes place on the bias board from where the signal is sent to the **D**igital **P**ulse **P**rocessor (DPP) in order to be digitized.

detector as they would get absorbed by the air. To ensure a vacuum environment, a turbomolecular pump has been used. Pressures as low as $4 \cdot 10^{-7}$ mbar could be reached. A circulated refrigerator is also connected to the setup, though it was not utilized during the performed measurements.

2.3.1 Design of detector holding structure

In order to minimize the backscattering effect due to the proximity of the copper detector-mount to the source, I designed a new detector holding structure. The new detector-mount, also made out of copper, enables the user to perform measurements placing the detector at different distances from the source. This allows to control to some extent the maximal incidence angle. The mount was fabricated by the Max Planck Physics Institute workshop. A major disadvantage of the new structure came to light when measurements (outside of this thesis' framework) at low temperatures were to be performed. Since the thermal contact to the cooling surface is poor, the detector could not be assumed to be cooled down. Figure 2.5 shows the old and the new detector-mounts.

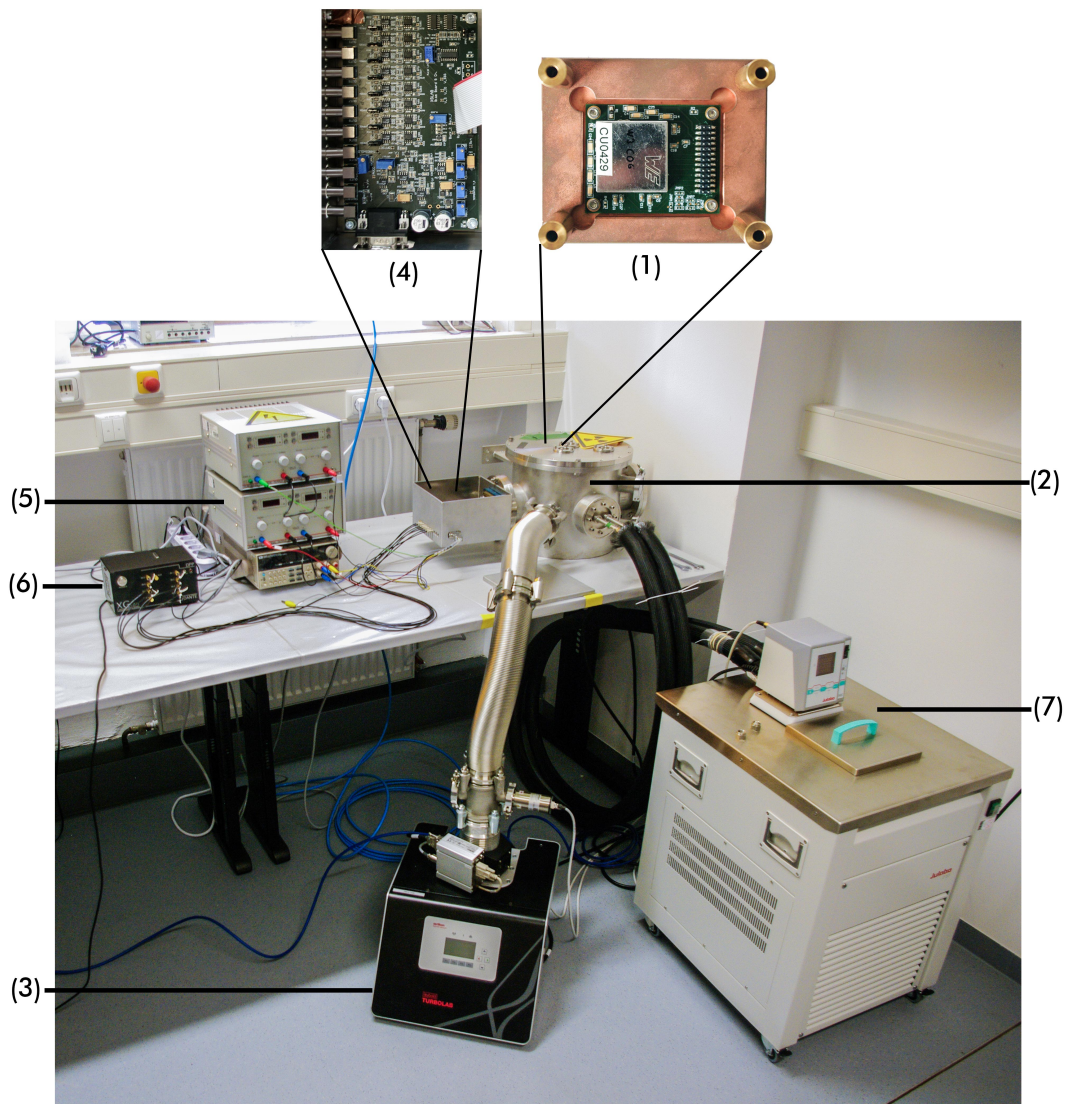


Figure 2.4: Experimental setup: (1) TRISTAN prototype detector framed on the copper mount structure, (2) vacuum chamber, (3) turbomolecular pump, (4) bias board, (5) DANTE DPP, (6) voltage supply, (7) cooling engine.

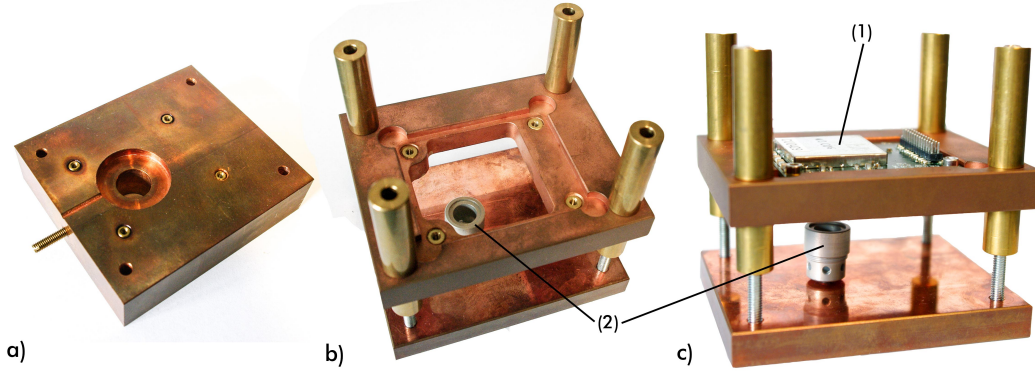


Figure 2.5: a) old detector-mount: the radioactive source was placed in the middle of the structure. b) new mount c) new mount with (1) TRISTAN prototype detector and (2) a dummy source installed.

2.4 Optimization of DAQ settings

Before the main measurement with the $^{83\text{m}}\text{Kr}$ source, the detector was exposed to a ^{55}Fe source in order to find the optimal threshold and peaking-time settings. These were later passed to the DAQ for the actual Krypton measurement. The ^{55}Fe isotope decays by electron capture to ^{55}Mn and emits (among other particles) three x-rays with the following energies:

	Energy / keV	relative probability
$K_{\alpha 1}$	5,89875	0.51
$K_{\alpha 2}$	5,88765	1
K_{β}	6,49045	0.205

Table 2.1: Main X-ray energies of ^{55}Mn [27]

As the $\text{Mn-}K_{\alpha 1}$ and $\text{Mn-}K_{\alpha 2}$ lines lie very close together, they can, for the purpose of the undertaken measurements, be assumed as one mono-energetic line of 5.9 keV.

Both x-ray peaks were fitted with a first-order polynomial and a Gaussian function. The corresponding graphs can be found in the appendix figs. A.1 and A.2.

2.4.1 Determination of the optimal peaking time

In silicon drift detectors, the electronic noise can easily spoil the detector's resolution. In order to prevent this, it is essential to choose an adequate peaking-time. The

peaking-time is the time the signal's leading edge takes to rise from zero to its maximum value. A short peaking-time value is essential if one wants to handle high count rates.

If the peaking time is chosen too low, the series noise from the preamplifier, caused by the **F**ield **E**ffect **T**ransistor (FET), becomes too important and lowers the resolution. For too high peaking-time values, the parallel noise component of the preamplifier takes over. The parallel noise is mainly due to the leakage current. The contribution of the noise to the signal has to be minimized by choosing a suiting peaking-time. [28, 29]

In order to optimize the peaking-time value, a 'sweep' measurement, that is a series of measurements with constant parameters with only the 'peaking-time' value being changed from one measurement to the next one, has been performed using the ^{55}Fe source. To check the peaking-time's influence on the detector resolution, the **F**ull **W**idth at **H**alf **M**aximum (FWHM) of the $\text{Mn-}K_{\alpha}$ peak was plotted as a function of the peaking-time. The presence of the second peak, $\text{Mn-}K_{\beta}$, allowed for a calibration of the energy scale. As one can see from figure 2.6, the best resolution for the $\text{Mn-}K_{\alpha}$ peak at room temperature is achieved for a peaking-time value of 800 ns. The detector reached a resolution of (182.8 ± 1.3) eV @ 5.9 keV at room temperature.

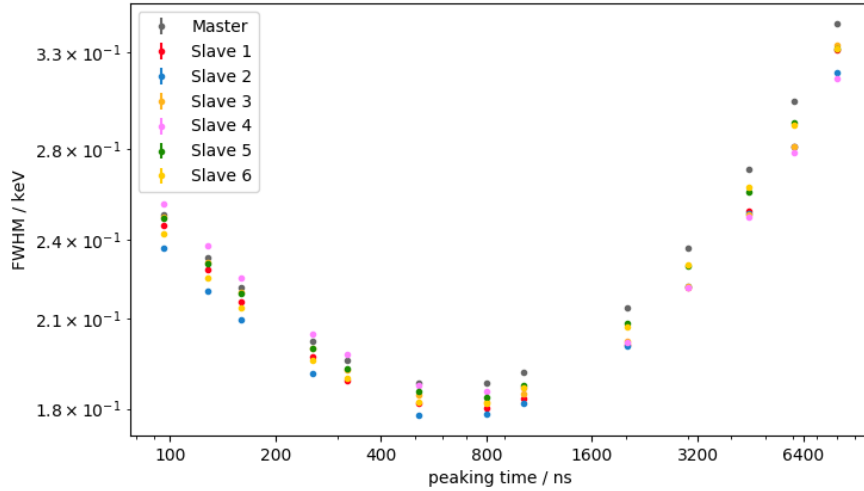


Figure 2.6: Peaking time optimization measurement. For all pixels, the best energy resolution of approximately 182 eV @ 5.9 keV at room temperature is attained for a peaking time value of 800 ns.

2.4.2 Determination of the optimal threshold value

The fast filter threshold value represents the minimal voltage rise during the peaking-time needed for an event to be registered by the DAQ. If set too low, the DAQ will register random electronic noise spikes and a noise peak will appear in the low energy range. On the other hand, if set too high, the baseline measurement becomes inaccurate as events below the threshold value are being discarded. [30]

In order to obtain the optimal threshold value, a second series of measurements without the ^{55}Fe source was required. This time the peaking-time was kept constant at a value of 800 ns, while the energy threshold was being varied. To be able to compare the different threshold values, each measurement had the same runtime of 300 seconds.

The recorded data can be seen in figure 2.7. The energy threshold chosen for the Krypton measurement has been determined by looking for the lowest threshold value at which the noise-peak was suppressed. For further measurements, an energy threshold of 95 ADC (**A**nalog to **D**igital **C**onverter - scale) was chosen. The obtained value can be interpreted as the minimal threshold value at a comparably low noise trigger rate [17].

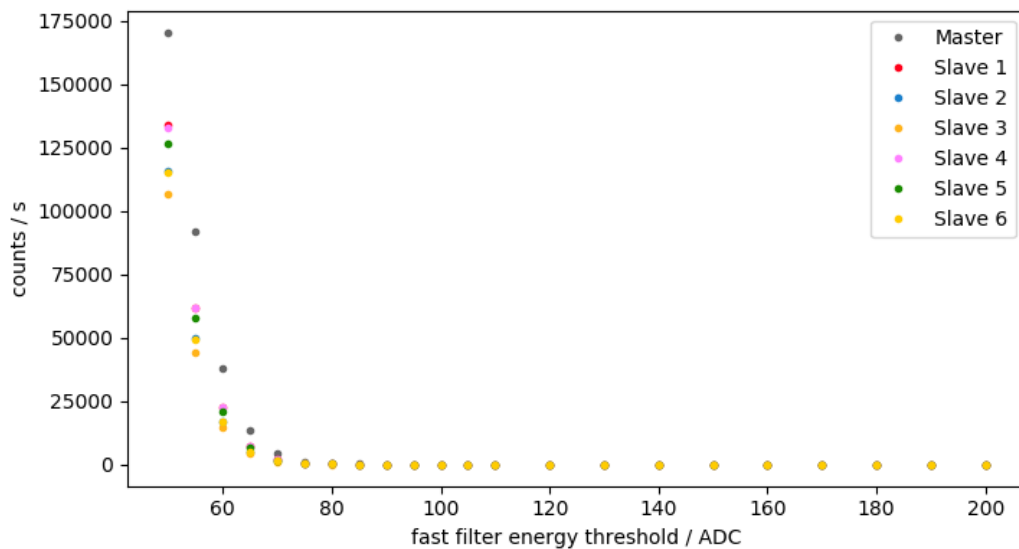


Figure 2.7: Energy threshold measurement. With no radioactive source, the bigger the setting of the energy threshold value, the fewer events are being registered by the detector. At low values, signals due to the electronic noise become dominant.

3

Krypton measurement

In the following chapter, the undertaken procedure in order to determine the dead-layer thickness will be presented. A short description of the $^{83\text{m}}\text{Kr}$ source and an argumentation why it is well suited for the dead-layer determination can be found in section 3.1. In order to evaluate the recorded Krypton data, a comparison with a simulated spectrum [17] was suited. After identification of the different peaks, an empirical model for the electron and photon detector response functions was developed. The individual analytic fit functions can be found in section 3.2. The determination of the photon peak positions allows for a precise calibration of the recorded spectrum which is being shown in section 3.3. This in turn is being used in section 3.5 to calculate the shift of the electron peaks compared to their theoretical position. In order to estimate the actual thickness of the dead-layer, a comparison to a theoretical calculation is necessary. The calculation as well as the final result are being presented in section 3.5.3. Section 3.4 also gives a brief overview over the detector's resolution and pixel homogeneity.

3.1 Dead-layer determination with Kr-83m

For the main measurement, an evaporated rubidium-krypton source was used. The source was produced at the Nuclear Physics Institute in Řež, Czech Republic. [31]

The rubidium decay scheme can be seen in figure 3.1. ^{83}Rb decays by electron capture to $^{83\text{m}}\text{Kr}$ with a half-life of $T_{1/2} = 86,2$ days. The $^{83\text{m}}\text{Kr}$ is still in an excited state and, having a half-life of 1,83 hours, is a source of monoenergetic conversion electrons, Auger electrons, γ - and x-rays. Because of the presence of γ - and x-rays, the Krypton source is very well suited for calibration measurements which can be performed in-situ. On the other hand, the emitted electrons can be used to investigate the detector dead-layer as it influences them differently compared to photons. Since the rubidium-krypton-source consist of a thin evaporated layer, the conversion electrons emitted from $^{83\text{m}}\text{Kr}$ do not lose much energy while escaping the source. Furthermore, $^{83\text{m}}\text{Kr}$ is a fitting source for the characterization of the TRISTAN detectors as there are electrons emitted in the energy range that will be analyzed in the final experiment employing tritium. [4, 32]

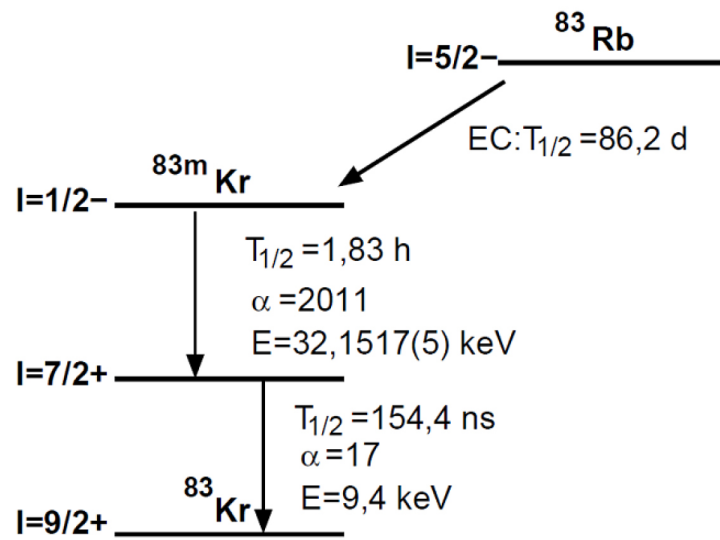


Figure 3.1: Rubidium-83 decay scheme [33]. ^{83}Rb decays to ^{83}Kr passing by the intermediate state of $^{83\text{m}}\text{Kr}$.

In order to identify the peaks in the recorded data, a comparison to a simulated spectrum [17] was necessary.

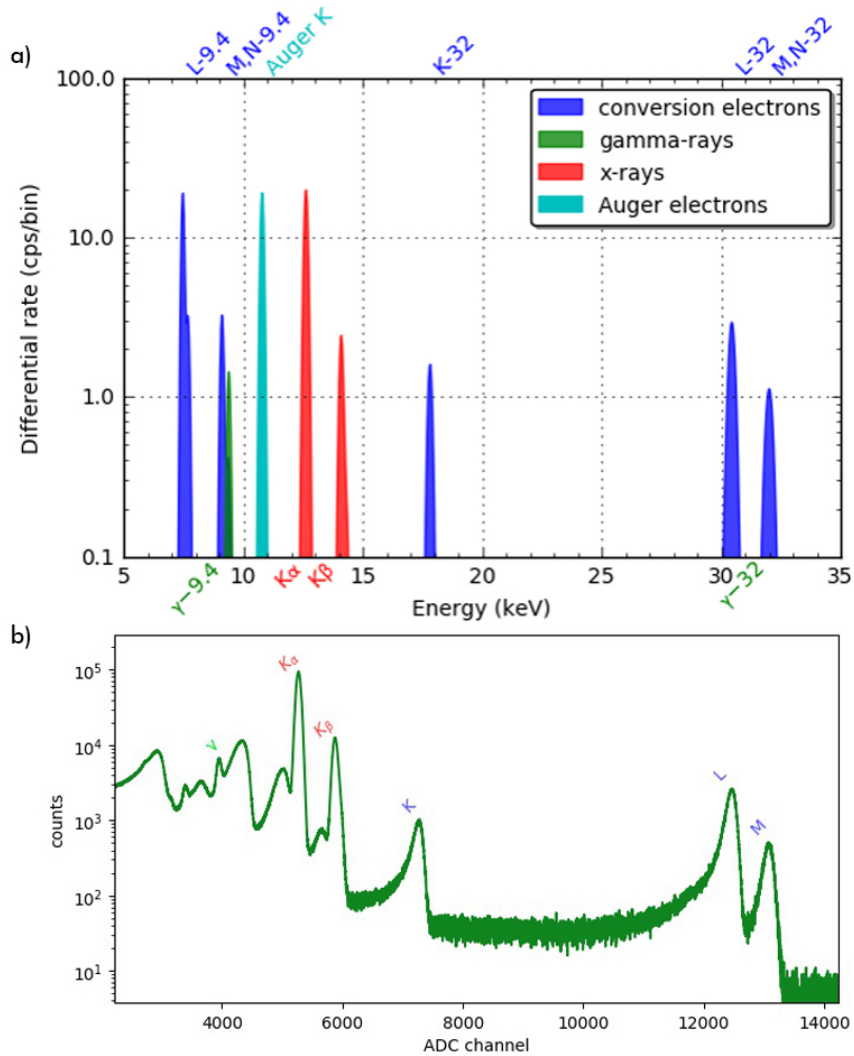


Figure 3.2: a) Theoretical distribution of the various peaks that can be found in the decay of Krypton [17] and b) recorded spectrum

Since $^{83\text{m}}\text{Kr}$ is an emitter of various particles including γ -rays, conversion electrons, x-rays and Auger electrons, a brief overview of their origin will be given.

Being in an excited state with an excitation energy of ≈ 41 keV, the $^{83\text{m}}\text{Kr}$ decays to its ground state in two steps. The two gamma transitions are characterized by deexcitation energies of approximately 32.2 keV and 9.4 keV. [32, 34]

The exact energies and the relative intensities of the γ -rays are presented in table 3.1.

	Energy / eV	relative intensity
γ	9405.7(6)	5.5(6)
γ	32151.6(5)	0.062(7)

Table 3.1: γ -rays in $^{83\text{m}}\text{Kr}$ decay [32]

The emission of conversion electrons can take place whenever γ -radiation is possible. During the process, the excited nucleus interacts electromagnetically with an orbital electron. For most elements, the probability for the interaction is highest for the inner K-shell and diminishes fast for the outer shells. Due to the energy gain from the γ , the orbital electron, now called a conversion electron, is ejected from the atom carrying the energy of the γ -ray minus its own binding energy. Considering that the γ -radiation has characteristic energies just as do the orbital electrons, the energy spectrum of the emitted conversion electrons is discrete. Since γ -rays are usually very energetic, the conversion electrons are characterized by a relatively high energy. [35]

As can be seen in table 3.2 for $^{83\text{m}}\text{Kr}$, the energies of the considered conversion electrons are not particularly high.

	Energy / eV	relative intensity
K	17824.2(5)	24.8(5)
L_1	30226.8(9)	1.56(2)
L_2	30419.5(5)	24.3(3)
L_3	30472.2(2)	37.8(5)
M_1	31858.7(6)	0.249(4)
M_2	31929.3(5)	4.02(6)
M_3	31936.9(5)	6.24(9)

Table 3.2: Most important conversion electrons in $^{83\text{m}}\text{Kr}$ decay [32]

As the emission of an orbital electron results in a hole in the electronic shell, the internal conversion process is followed by the emission of an x-ray and/or Auger electron in order to fill the vacancy in the electronic orbitals.

X-rays are emitted when an electron from a higher shell falls to a lower energy level. The energy difference is released in the form of electromagnetic radiation, called x- or Röntgen-radiation after Wilhelm Röntgen who discovered it in 1895 [36]. Since the electron energy levels in an atom are discrete, x-rays from a given atom present a characteristic energy spectrum. The characteristic energies of the studied $^{83\text{m}}\text{Kr}$ x-rays lines are presented in table 3.3.

	Energy / eV	relative intensity
$K_{\alpha 1}$	12648.002(52)	9.1(3)
$K_{\alpha 2}$	12595.424(56)	4.70(19)
$K_{\beta 1}$	14112.815(80)	1.27(5)
$K_{\beta 2}$	14315.0(24)	0.167(6)
$K_{\beta 3}$	14104.96(11)	0.65(3)

Table 3.3: Most important x-rays in $^{83\text{m}}\text{Kr}$ decay [32]

However, the electron falling down from the higher energy level into the hole on a lower level can also transfer its energy to another electron from an outer shell. If the transferred energy is bigger than the binding energy of the outer shell electron, the latter gets ejected from the atom as an Auger electron [37]. The process is named after Pierre Auger who is credited for discovering the effect in 1892. The name attribution is controversial, since Lise Meitner observed and described the Auger effect independently shortly before Pierre Auger [38].

3.2 Empirical model for electron & photon peaks

In order to evaluate the recorded spectrum, the different peaks had to be described analytically. For this purpose, different functions were fitted to the data using Python's `lmfit` [39].

3.2.1 Photon response

For the photon peaks, the used fit functions were very simple, but different approaches had to be applied depending on the evaluated peak. To fit the 9-keV- γ peak, a constant, an exponential, a step S and a Gaussian G function were used.

$$S = A_{\text{step}} \cdot \text{erf} \left(\frac{E - E_0}{\sqrt{2} \cdot \sigma} \right) \quad (3.1)$$

$$G = A_{\text{gauss}} \cdot \exp \left(\frac{(E - E_0)^2}{2 \cdot \sigma^2} \right) \quad (3.2)$$

While the 9.4 keV γ -peak did not present a high statistic, it was important for the calibration, since the K_α and K_β peaks lie closely together. The γ -peak is situated on the tail of a bigger peak coming from an Auger electrons. In order to approximate the Auger electron peak's tail, the exponential function was used. The background was fitted with a constant, while the γ -peak itself was matched with a Gaussian function (eq.3.2), whose mean was defined as the peak position. The final fit as well as the single functions can be seen in figure 3.3.

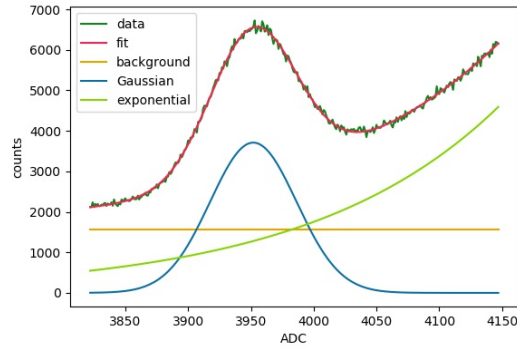


Figure 3.3: Fit functions of the γ -peak. A simple Gaussian function and a constant were used in order to obtain an adequate fit of the γ -peak. The tail of the bigger peak was approximated with an exponential function.

Since the K_α and K_β peaks are composed of multiple lines, a different approach to fit the peaks was attempted. A first-order polynomial was overlaid with a step (eq.3.1) and multiple Gaussian functions (eq.3.2), one for every (major) line contributing to the peak. The first order polynomial was used to approximate the background, while the step function accounts for the minor asymmetry of the peaks. With the table values from 3.1, the relative intensities and positions of the peaks were passed to the fitting algorithm as a fixed parameter for the amplitudes and positions of the Gaussian functions. In doing this, the position of every peak was defined as the mean of the corresponding Gaussian function. Every data point was weighted by the square root of the events it represents. Since the positions of the secondary Gaussian functions describing the lower intensity lines in the K_α and K_β peaks were restrained by the position of the Gaussian matching the main line, they were not a free fit parameter. Naturally, they were not taken into account in the calibration process. The fitted models can be seen in figure 3.4.

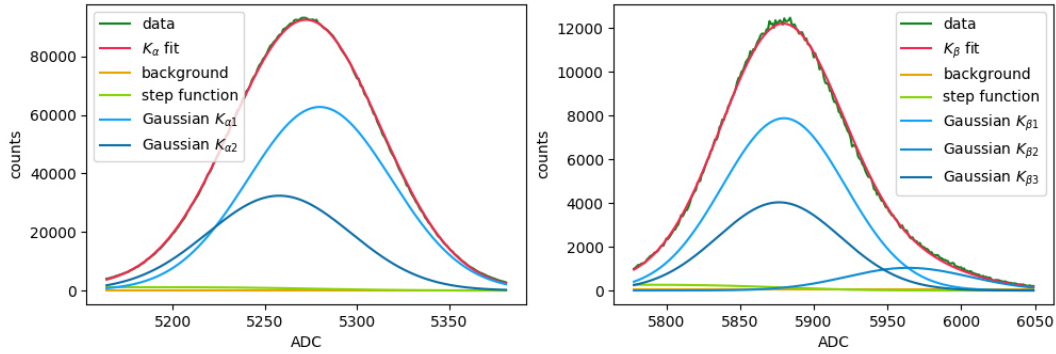


Figure 3.4: Fit functions of the K_α and K_β peaks. Being composed of multiple lines, both peaks were fitted with Gaussian functions whose relative amplitudes and positions were fixed by the tabular values. Furthermore, a first degree polynomial and a step function were included in order to minimize the influence of the background and to account for the slight asymmetry of the peaks.

3.2.2 Electron response

For the conversion electrons, the fit function consists of a first order polynomial (line), a step function S , multiple Gaussians G and functions D taken from [24] describing the low energy tail of the electron peaks.

$$D = A_{\text{diff}} \cdot \exp\left(\frac{E - E_0}{\beta}\right) \cdot \left(1 - \text{erf}\left(\frac{E - E_0}{\sqrt{2} \cdot \sigma} + \frac{\sigma}{\sqrt{2} \cdot \beta}\right)\right) \quad (3.3)$$

Again, the first order polynomial was employed in order to approximate the background, the step (eq.3.1) and low-energy-tail (eq.3.3) functions were adjusted to describe the asymmetry of the peak. This asymmetry is mainly due to the dead-layer and charge sharing effect. The same as for the x-ray peaks, the relative amplitudes and peak positions of the conversion electron peaks were determined using the tabular values from 3.2 and passed to the fitting algorithm as a fixed parameter for the fitting of the Gaussian functions (eq.3.2). Consequently, the actual peak position was defined as the mean of every Gaussian function. Once more, every data point was weighted by the square root of the events. Since the positions of the secondary lines of the L- and M-peak were yet again not a free fit-parameter only the position of the most important lines, namely L_3 and M_3 , will be referenced during further analysis.

Figure 3.7 shows the entire krypton spectrum with the fitted electron and photon peaks.

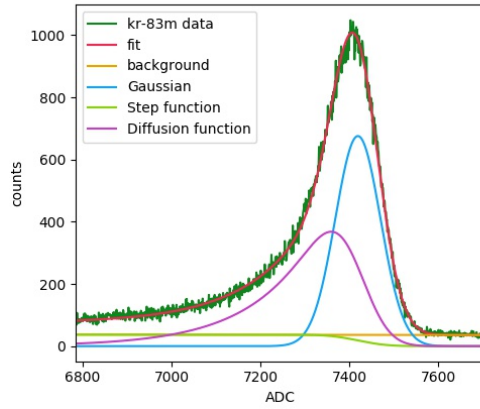


Figure 3.5: Fit of the K-32 conversion electron peak

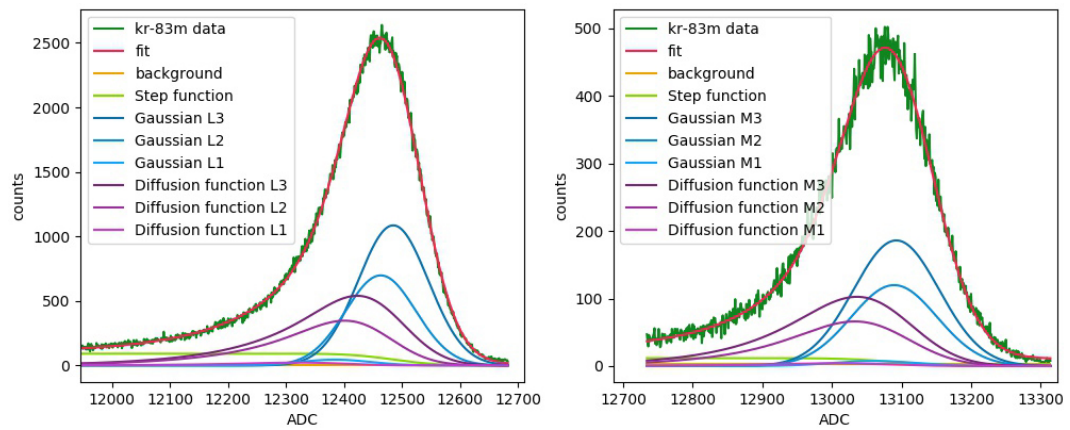


Figure 3.6: Fit of the $L_{1,2,3}$ -32 and $M_{1,2,3}$ -32 conversion electron peak

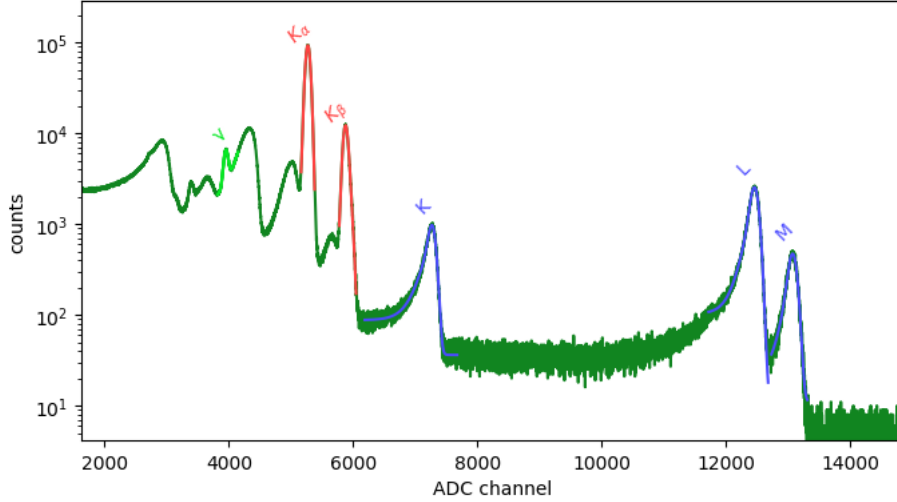


Figure 3.7: Uncalibrated $^{83\text{m}}\text{Kr}$ decay spectrum together with the fitted peaks. (green: γ , red: K_{α} & K_{β} , blue: K, L, M conversion e^{-})

3.3 Energy calibration

To be able to analyze the shift of the electron peaks compared to their theoretical position, a calibration of the **A**nalog-**D**igital-**C**onverter (ADC) scale was necessary. With the above mentioned empirical fit functions the ADC-position of the photon and electron peaks could be determined. As already mentioned in section 3.2, given the complex shape of the single peaks, the peak position was defined as the mean of the fitted Gaussian function.

To calibrate the ADC scale the positions of the γ - and x-ray peaks could be used since unlike the electrons, their detected energy was not affected by the dead-layer. Only the photon peaks whose position was a free parameter during the fit process (9.4-keV- γ , $K_{\alpha 1}$, $K_{\beta 1}$) were used for the calibration. Since the deviation from linearity on the ADC scale is guaranteed by the manufacturer to be smaller than 0.1% [17], a linear calibration fit, shown in figure 3.8, was chosen. The calibration curve was obtained by the least square method minimizing the squared distance of the various point with respect to the curve.

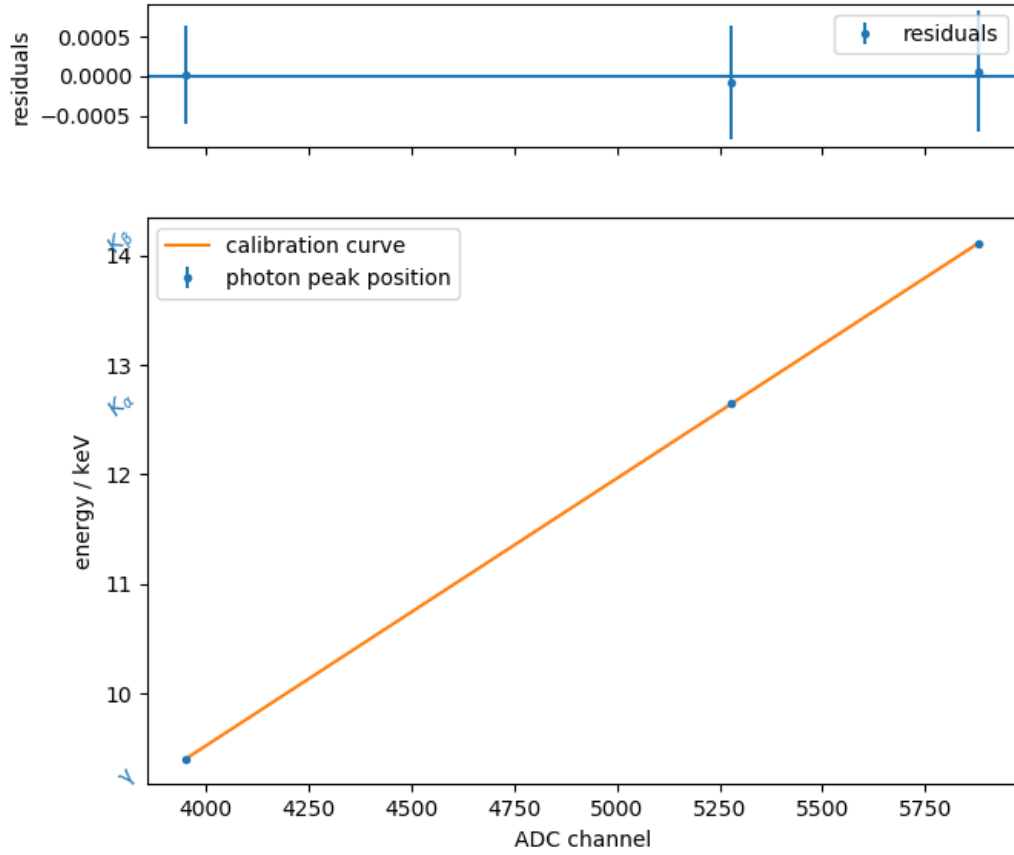


Figure 3.8: The calibration curve obtained with the peak positions of the γ - and x-rays allows to convert the ADC-scale into energy / keV.

The error bars on the photon peaks ΔE_{keV} are calculated from the standard errors of the peak position on the ADC-scale ΔE_{ADC} and the standard errors for the slope $\Delta m = \sigma_m^2$ and offset $\Delta y_0 = \sigma_{y_0}^2$ of the calibration curve as well as their correlation $\sigma_m \cdot \sigma_{y_0}$ (eq.3.4). All values can be obtained using the covariance matrix of the fit.

$$\Delta E_{\text{keV}} = \sqrt{(\Delta E_{\text{ADC}} \cdot m)^2 + (\Delta m \cdot E_{\text{ADC}})^2 + (\Delta y_0)^2 - (2 \cdot \sigma_m \sigma_{y_0} E_{\text{ADC}})} \quad (3.4)$$

The so calibrated $^{83\text{m}}\text{Kr}$ decay spectrum is shown in figure 3.9 together with the theoretical lines (blue) of the analyzed peaks. The theoretical lines represent the tabular values tables 3.1 to 3.3 which obviously do not include the observed electrons' energy shift. For the peaks composed of multiple lines, the represented theoretical line was calculated by a weighted average. The shift of the electron peak positions is now apparent and will be further discussed in section 3.5.2.

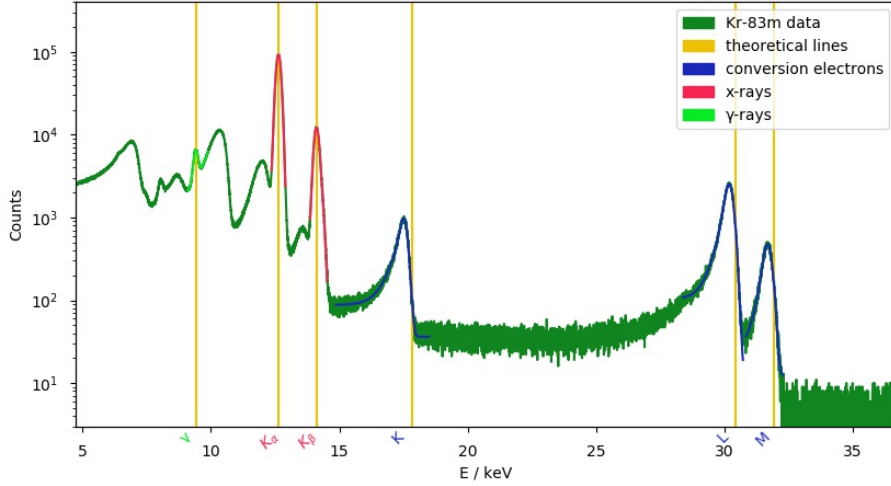


Figure 3.9: Krypton-83m decay spectrum calibrated with the γ - and x-ray lines. While the γ - and x-ray peaks do correspond to their theoretical value, the peaks of the conversion electrons are evidently shifted to lower energies compared to their theoretical value.

3.4 General performance

Before exploring the dead-layer thickness, the general performance of the detector exposed to the emission of the Kr-83m calibration source was investigated. Here, the focus is on the energy resolution and pixel homogeneity.

3.4.1 Energy resolution

As the signature of the sterile neutrino is a small kink-like feature in the energy spectrum of the beta electrons, an important design parameter is the energy resolution of the detector. The measurement with Kr-83m allows to compare the resolution of the detector for electrons and photons. As expected, the width of the electron peak is broadened due to the energy loss in the dead-layer. Another effect is that some electrons backscatter from the detector surface and only deposit a fraction of their original energy. It should be also noted here, that no multiplicity cut has been made to the data. This implies a possible presence of charge sharing i.e. interactions that happen on the border between two pixels and generated charge carriers that were collected by two or even three different pixels. The pixels register these as separate events with an inferior energy to the one of the incoming particle. Ap-

plying a multiplicity cut would likely improve the resolution. This is up to further investigation.

Figure 3.10 shows the energy resolution of photon and electron peaks relative to their energy. The full width at half maximum was determined differently for photons and electrons. Since the fit of the photon peaks almost exclusively consists of Gaussian functions, the FWHM was calculated using only the standard deviation value σ of the fitted Gaussians.

$$\text{FWHM} = 2\sqrt{2 \cdot \ln 2} \cdot \sigma \quad (3.5)$$

The calculation of the error-bars was done the same way as for the calibration curve (eq.3.4) and can be found in the appendix (eq.A.1). The FWHM of the x-ray peaks is lightly underestimated, since they contain multiple lines.

For the conversion electron peaks, the approach had to be modified, since their peaks are considerably broadened and asymmetric due to the above mentioned effects. The FWHM of the electron peaks was determined by measuring the width of the fitted function at half of its maximal value. The background was subtracted in the calculation of the 'half-maximum'. The corresponding figure can be found in the appendix A.3. Leaving the peak broadening aside, the error-bars were calculated in exactly the same way as for the photon peaks and were probably underestimated. Figure 3.10 shows the obtained FWHM of all fitted peaks including the calculated error-bars.

One can observe that, as expected, the FWHM grows with an increasing energy of the incoming particle. The conversion electron peaks are also clearly characterized by broader FWHM compared to the photon-generated peaks. The under- and over-estimations mentioned above cannot be the only reason for this disparity.

In figure 3.10 the green curve represents the theoretical broadening due to the electronic noise, as well as statistical fluctuations in the amount of generated charge carriers described by equation 3.6 which makes use of the information introduced in section 3.4.1. A pair creation energy for silicon of $E_{\text{pair}} = 3.64 \text{ eV}$, a Fano factor of $F = 0.124$ [20] and an equivalent noise charge of $n_{\text{ENC}} = 9$ [17] were assumed.

$$\text{FWHM}_{\text{theo}} = 2\sqrt{2 \cdot \ln 2} \cdot E_{\text{pair}} \cdot \sqrt{n_{\text{ENC}}^2 + \frac{F \cdot E_{\text{peak}}}{E_{\text{pair}}}} \quad (3.6)$$

As one can see, all peaks are broader than their theoretical minimal width. This can be attributed to an underestimation of the electronic noise, charge sharing as well as the dead-layer in the case of electrons. Taking into account the influence of the dead-layer, the much broader FWHM of the electrons compared to the photons can be explained.

Although a cooling machine is connected to the setup, it was not employed during the measurements and the detectors were left at room temperature. Performing the

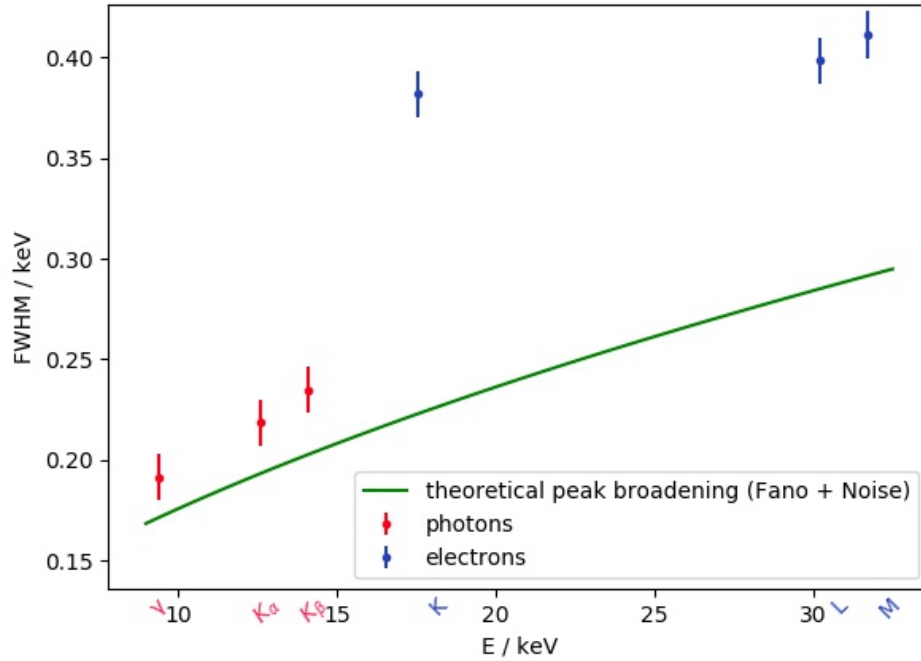


Figure 3.10: FWHM of the recorded peaks over the energy of the incoming particles. The theoretical broadening due to the Fano limit and the electronic noise was also included.

measurements at lower temperatures significantly reduces the electronic noise and allows for longer shaping times which results in a better resolution.

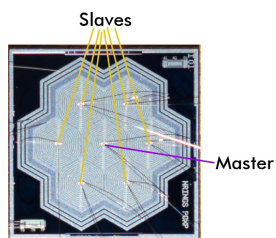


Figure 3.11: Pixel map.

3.4.2 Pixel homogeneity

Finally, a similar behaviour of all pixels significantly facilitates the final complex sterile neutrino analysis. In this measurement the performance of all seven pixels was compared. Because of its position (figure 3.11), the central pixel (Master), registered more events than the surrounding pixels (Slaves). The main reason for this increased count rate is probably the lack of the multiplicity cut pointed out in section 3.4.1, as the Master pixel has the most neighbouring pixels. Since the effect of charge sharing deteriorates the resolution, it can also be seen when looking at figure 3.12 presenting the FWHM of different pixels. The peaks of the Master pixel indeed do have wider FWHM compared to other pixels. The FWHM mean value and its standard error σ_{FWHM} can be found in table 3.4. It has to be noted that for the calculation of the mean values and their standard deviations, the individual errors were not considered.

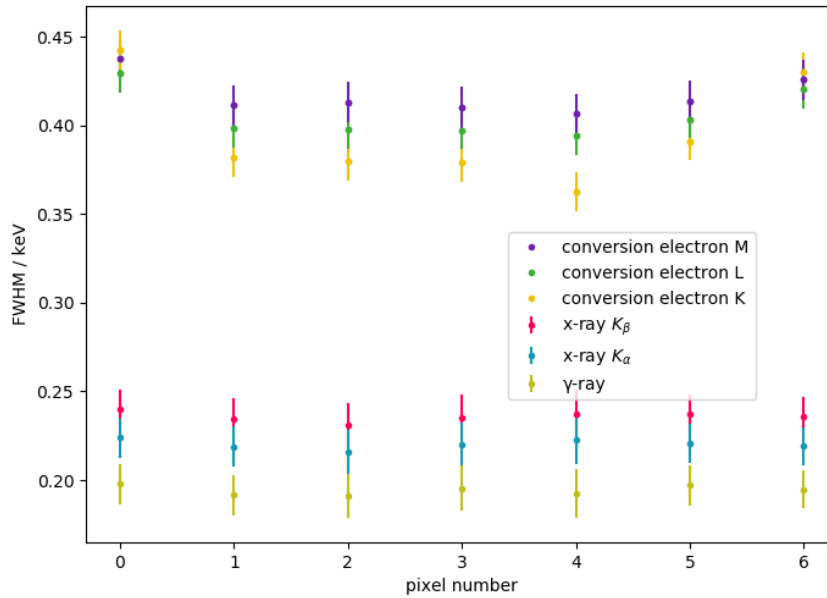


Figure 3.12: FWHM of analyzed peaks, different pixel.

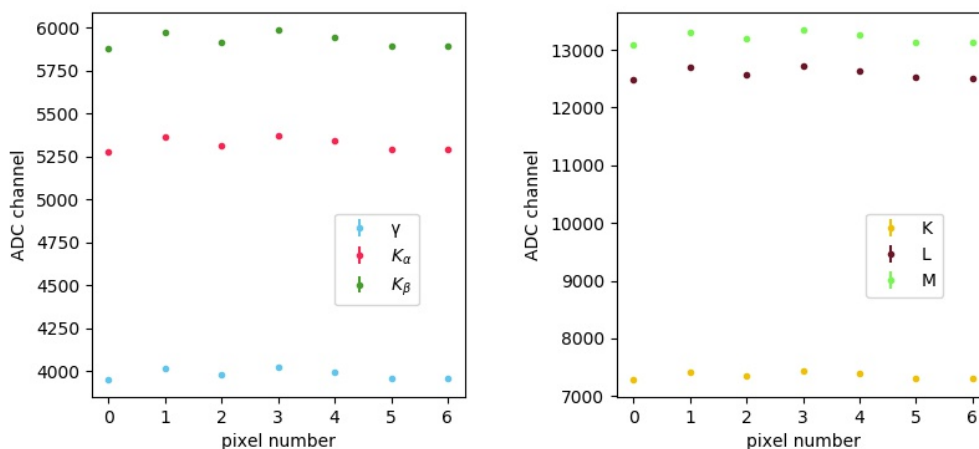


Figure 3.13: ADC-scale peak positions of photons and electrons, different pixels.

When analyzing the peak positions of the different pixels on the ADC-scale, one can clearly see in figure 3.13 that they are collectively shifted from pixel to pixel. The fact that the shift between pixels shows a similar trend in both figures representing the photon and electron peaks is reassuring. Table 3.4 shows the mean peak position values as well as their standard deviation error σ_{ADC} .

peak	ADC	σ_{ADC}	%	FWHM / eV	σ_{FWHM}	%
9.4-keV- γ	3984.43	± 10.75	0.27	194	± 1.0	0.5
$K_{\alpha 1}$	5323.03	± 14.40	0.27	220	± 1	0.5
$K_{\beta 2}$	5928.10	± 16.12	0.27	236	± 1	0.5
K	7356.21	± 22.01	0.30	395	± 11	2.8
L_3	12593.15	± 35.29	0.28	406	± 5	1.3
M_3	13205.56	± 37.42	0.28	417	± 4	1.0

Table 3.4: Variations across pixels in the peak positions on the ADC-scale

Because of the lack of peak position stability from pixel to pixel, every pixel obviously requires its own calibration. The slopes and offsets of the calibration curves, which can be seen in figs. A.4 and A.5 in the appendix were found to have a standard deviation error of 0.27% and 0.39% respectively. The slope's standard deviation noticeably corresponds to the standard errors of the peak positions in table 3.4.

3.5 Determination of the dead-layer thickness

As already mentioned in section 3.1, photons and electrons present a different behaviour when they are being absorbed by the silicon drift detector. While the photons will travel through the dead-layer without losing any energy, electrons will always suffer small energy losses in the dead-layer.

3.5.1 General idea

The dead-layer is formed by the irregularities at the borders of the detector due to the semiconductor's doping and ohmic contacts to supply the bias voltage and connect the read-out electronics. The negative charge carriers generated in the dead-layer will not (or only partly) be collected by the anode, since the internal electric field and the doping arrangement is not strong enough to extend the depletion volume into this region. Though it has been shown that an important fraction of the charge carriers generated in the dead-layer can reach the depletion volume by diffusion and thus contribute to the recorded signal [40].

As photons do not carry an electrical charge, the probability that they pass the dead-layer without interacting with it is a lot higher than it is for electrons. On the other hand, if photons do interact with the dead-layer, as their interaction with matter can be assumed point-like, they will deposit their entire energy in it. On the contrary, electrons, being charged particles, will steadily lose energy via coulombic interactions with atomic electrons from the dead-layer. Because of this, the energy that the electrons deposit in the bulk semiconductor is always inferior to their initial energy. As a consequence, the observed energy peaks of the photons do correspond to their initial energy whereas the peaks of the electrons are shifted with respect to their theoretical energy. An illustration of this phenomenon is depicted in figure 3.14.

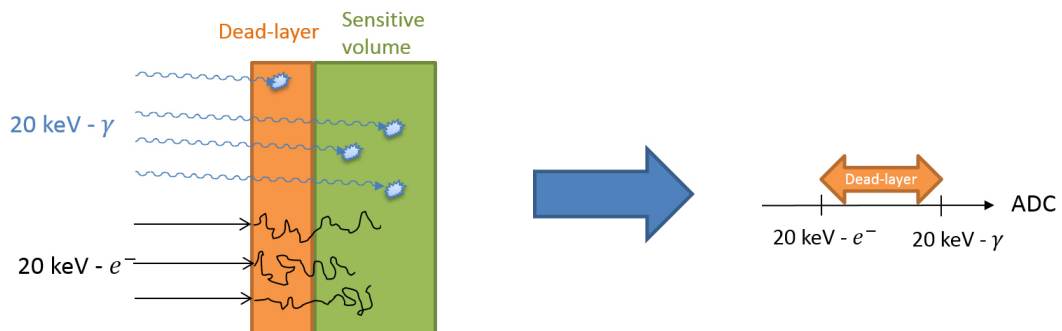


Figure 3.14: Influence of the dead-layer on the peak position of photons and electrons of the same energy [17]. The electron peak position is shifted compared to the photon peak position of the same initial energy.

As can be seen in figure 3.9, the dead-layer indeed distorts the electron-energy spectrum. Since in the TRISTAN experiment the electrons' energy has to be known with great precision, a thin dead-layer is an essential requirement.

3.5.2 Observed shift of electron peak position

As pointed out in section 3.3, the electron peak positions are shifted away from their theoretical energy values. Besides the calibration curve, the theoretical lines of the electron peaks over their position on the ADC-scale were plotted in figure 3.15. It can be seen that the measured electron peak positions are not situated on the calibration curve. If their ADC-scale value corresponded to their theoretical energy value, the electron peak positions would lie on the calibration curve, however they are shifted to the left. This means that a peak of energy E , which should appear in the ADC-bin X , actually emerges in an ADC-bin $x < X$. This ADC-bin x gets converted by the calibration curve to an energy $e < E$.

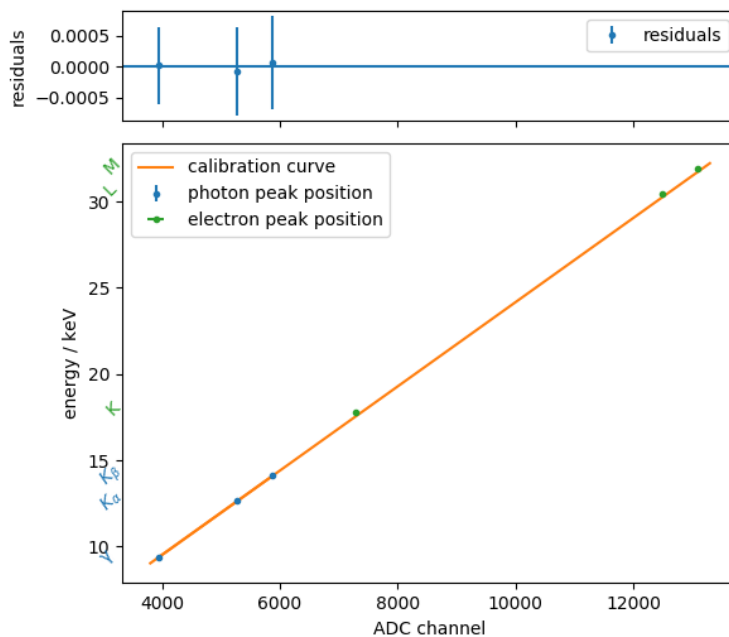


Figure 3.15: Calibration curve obtained with the photon peak positions overlaid with the measured electron peak positions. As expected, the electron peak positions are slightly shifted to lower ADC-values with respect to the calibration curve.

The shift of the electron's peak positions was calculated using the following equation:

$$Shift_{\text{keV}} = E_{\text{table, keV}} - (E_{\text{ADC}} \cdot m + y_0) \quad (3.7)$$

with $E_{\text{table, keV}}$ being the table value of the electron's energy, E_{ADC} its ADC-scale bin and m and y_0 the slope and offset of the calibration curve respectively. The error-bars of the energy shift were calculated as follows:

$$\Delta Shift_{\text{keV}} = \sqrt{(\Delta E_{\text{ADC}} \cdot m)^2 + (\Delta m \cdot E_{\text{ADC}})^2 + (\Delta y_0)^2 - (2 \cdot \sigma_m \sigma_{y_0} E_{\text{ADC}})} \quad (3.8)$$

In the performed Krypton measurement the electrons' maximal angle of incidence was only controlled by the detector-source distance and could reach a maximal value of $\theta = 38^\circ$. Given that at higher incidence angles, the electron's path across the dead-layer increases, they are more likely to deposit more of their energy in it. This has to be taken into account when calculating the dead-layer thickness.

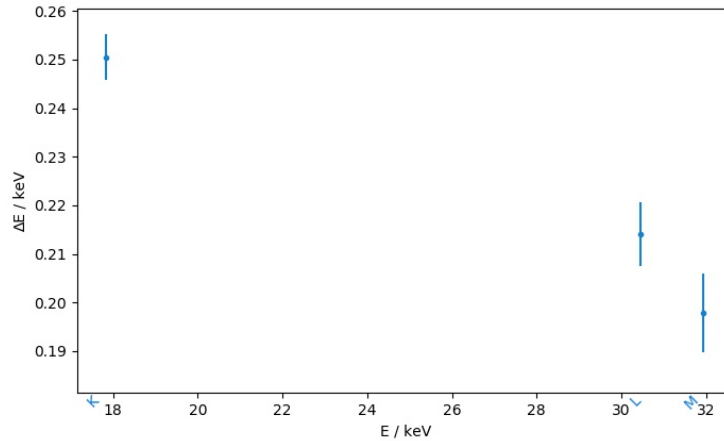


Figure 3.16: Shift of the electron peak position as a function of energy, pixel two.

It becomes apparent in figure 3.16 that the higher the initial energy of the electrons, the smaller the amount of energy deposited in the dead-layer. This corresponds with our expectations, since the mean free path of the electrons is expected to increase with increasing kinetic energy, whereas the stopping power of SiO_2 and Si , that both make up the dead-layer, was found to decrease with increasing energy[41] (in the considered energy range). Thus, lower energy electrons are more likely to interact with particles in the dead-layer and consequently lose part of their energy that will not be collected by the read-out electronics.

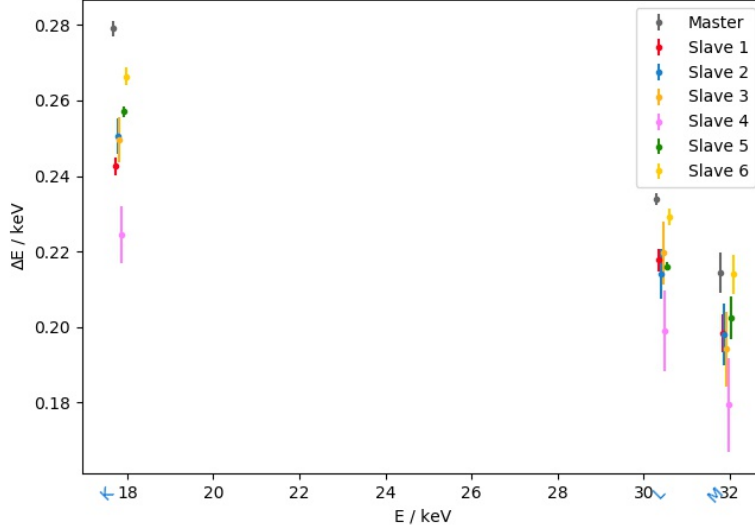


Figure 3.17: Shift of electron peak position as a function of energy. In the above graph the x-values (energy) of the different pixels were scattered around the actual energy value in order to compare the error-bars of the different pixels.

When comparing the energy shift of all pixels from figure 3.17, one can see that there is an important disparity. For instance, the Master pixel presents the highest energy shift among all pixels. This is probably again due to the charge sharing effect that is most important for the Master pixel. Although one should also consider that since the $^{83\text{m}}\text{Kr}$ source was centered with respect to the detector, the maximal incidence angle is lower for the Master pixel than it is for the Slaves. As mentioned above, this should reduce the influence of the dead-layer on the energy shift for the Master pixel compared to the Slave pixels. The relatively big error-bars on electron peak positions' shift of the Slave pixels 2-4 can be attributed to the important uncertainty of their calibration curve's slope A.5. The mean values of the electron peak position shift as well as their standard deviations are presented in table 3.5.

peak	shift _{eV}	σ_{shift}	%
K	252.8	± 6.6	2.6
L_3	218.5	± 4.2	1.9
M_3	200.1	± 4.6	2.3

Table 3.5: Mean shift of the electron peak positions of all 7 pixels

3.5.3 Comparison to theoretical model

Commonly, the dead-layer is stated in units of length. In order to obtain the dead-layer thickness from the observed energy shift, a theoretical calculations using the Bethe-Bloch formula (eq.3.9) was performed. [42]

$$-\frac{dE}{dx} = \frac{4\pi}{m_e c^2} \cdot \left(\frac{nz^2}{\beta^2}\right) \cdot \left(\frac{e^2}{4\pi\epsilon_0}\right)^2 \cdot \left[\ln\left(\frac{2m_e c^2 \beta^2}{I \cdot (1 - \beta^2)}\right) - \beta^2\right] \quad (3.9)$$

with m_e being the electron's mass, c the speed of light, n the electron density, ϵ_0 the electric constant, I the excitation potential and $\beta = \frac{v}{c}$ with v being the electron's velocity. The absorbing material was assumed to be entirely composed of silicon, even though a thin layer of ≈ 10 nm of SiO_2 is also part of the dead-layer. An electron density of $n_{\text{Si}} = 6.99 \cdot 10^{29}$ electrons/ m^3 and excitation potential $I_{\text{Si}} = 173$ eV were adopted for the calculation. The electron is constantly being slowed down when passing the dead-layer, but since the variation of its velocity is smaller than 0.02%, it was assumed to be constant. The obtained dead-layer thicknesses are presented in table 3.6 and were illustrated in figure 3.18.

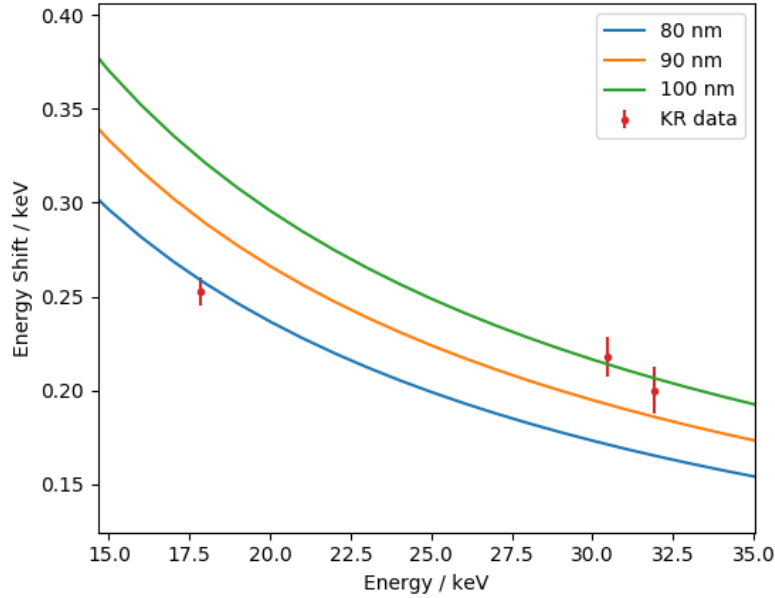


Figure 3.18: The energy loss calculated with the Bethe-Bloch formula was computed for dead-layer thicknesses in the range of 80 to 100 nm. The resulting plot was overlaid with the recorded average energy loss of the $^{83\text{m}}\text{Kr}$ conversion electrons.

peak	shift /eV	-dE/dx (eV/nm)	dead-layer /nm
K	252.8	3.236	78.2
L_3	218.5	2.138	102.0
M_3	200.1	2.063	96.9

Table 3.6: Dead-layer thicknesses obtained with the Bethe-Bloch formula 3.9.

One can see that the model suggests a thicker dead-layer considering the more energetic L_3 and M_3 electrons as compared to the K electrons. Averaging the calculated thicknesses, one obtains a result of (92.4 ± 7.2) nm for the dead-layer of the investigated prototype detector.

Since the dead-layer has no exactly defined border with the detector-volume, its estimated thickness strongly depends on the model that is employed for its calculation. For example, the Bethe-Bloch formula assumes a uniform absorption material, which obviously is not applicable to the dead-layer of a real SDD. This supposition underestimates the dead-layer thickness, since, as mentioned in section 3.5.1, the dead-layer is not completely inactive. Charge carriers from a certain part of the dead-layer do contribute to the recorded signal, as they can diffuse into the depletion zone [40]. On the other hand, the fact that the Bethe-Bloch formula assumes a straight line trajectory of the electrons across the dead-layer, overestimates the calculated thickness. Actually, the electron's momentum vector changes constantly with every interaction in the dead-layer as has been schematically shown in figure 3.14. Consequently, the electron's path across the dead-layer is longer than it would be if it crossed the layer in a straight line. Furthermore, the Bethe-Bloch formula assumes that the electrons hit the dead-layer at normal incidence. Supposing a straight line trajectory, the path of electrons with the maximal incidence angle of approximately 38° is 25% longer than for normal incidence, which also leads to an overestimation of the actual dead-layer thickness.

Due to the complexity of the problem, more sophisticated models clearly need to be developed for a more accurate estimation of the dead-layer thickness.

4

Conclusion & outlook

The TRISTAN project aims to upgrade the KATRIN setup in approximately five years when the ongoing neutrino mass measurements will be concluded. The upgraded setup will allow the search for keV-range sterile neutrinos. Among other components, the detector and the read-out system have to be improved since much higher count rates will be required as the whole tritium β -decay spectrum will be analyzed. The main focus of this work was the estimation of the TRISTAN prototype silicon drift detector's dead-layer thickness.

The prototype detector was investigated using a radioactive $^{83\text{m}}\text{Kr}$ source. For this purpose, a novel detector mount was designed to mitigate the issue of electrons backscattering from the previously employed detector frame. The basic settings of the data acquisition system were also optimized. In order to evaluate the recorded spectrum, empirical models for the photon and electron peaks were developed. The undertaken measurement assured a good performance of the prototype detector with an electron source. The analyzed conversion electrons had initial energies in the range between 18 and 32 keV and deposited on average 250 to 200 eV in the dead-layer. Comparing these results to a simple calculation using the Bethe-Bloch formula allowed to estimate the dead-layer thickness to approximately (92.4 ± 7.2) nm. This value does correspond to the current reference value of 80 nm [17]. Overall, the experiment constitutes a proof-of-concept of the prototype silicon drift detector and the method to determine its dead-layer thickness. The performed analysis assured that both the calibration and dead-layer determination are feasible using a $^{83\text{m}}\text{Kr}$ source.

Performing a multiplicity cut on the recorded data could allow for a more precise calibration and would likely decrease the calculated shift of the electron peak positions. Future proceedings will include the characterization of detectors produced with special techniques to reduce the dead-layer thickness and the comparison to simulations based on sophisticated entrance window models. For this purpose, MONTE CARLO based softwares like GEANT4 or KESS, which is made available from the KATRIN collaboration, could be employed.

Acknowledgements

First, I would like to thank Prof. Dr. Susanne Mertens for presenting me with the opportunity to do my bachelor's thesis in her group as well as her support along the way. I am also grateful to the Max Planck Society for assuring the necessary research facilities and to the Nuclear Research Institute in Řež for providing the employed krypton source. Further, I would like to thank Daniel, Tim, Thibaut and the other members of the MPP group for their assistance, encouragement and pleasant work environment.

A

Appendix

A.1 Second chapter appendix

In section 2.4.1 in order to optimize the peaking time value that was later passed to the data acquisition software for the krypton measurement, the full width at half maximum of the Mn- K_α peak was determined for different peaking times. Figures A.1 and A.2 show the recorded Fe⁵⁵ energy spectrum for a peaking time value of 800 and 8000 ns respectively.

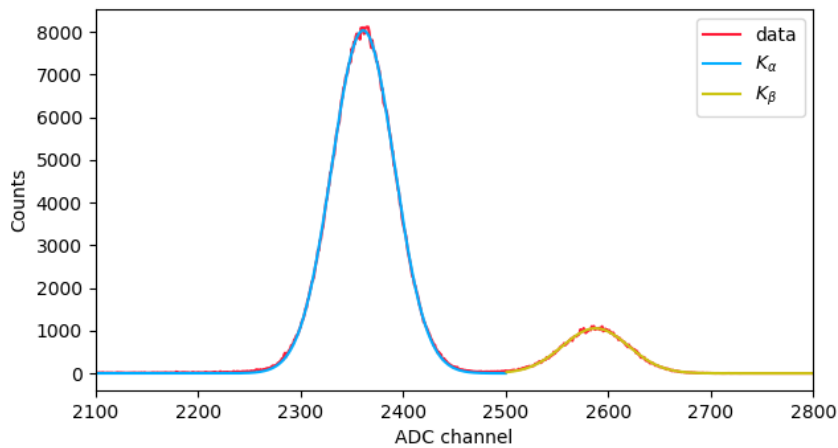


Figure A.1: Fe⁵⁵ decay spectrum for a peaking time value of 800 ns. Fit of the Mn- K_α and Mn- K_β peaks. For the peaking time value of 800 ns, the best resolution at room temperature was obtained amounting to 182 eV @ 5.9 keV.

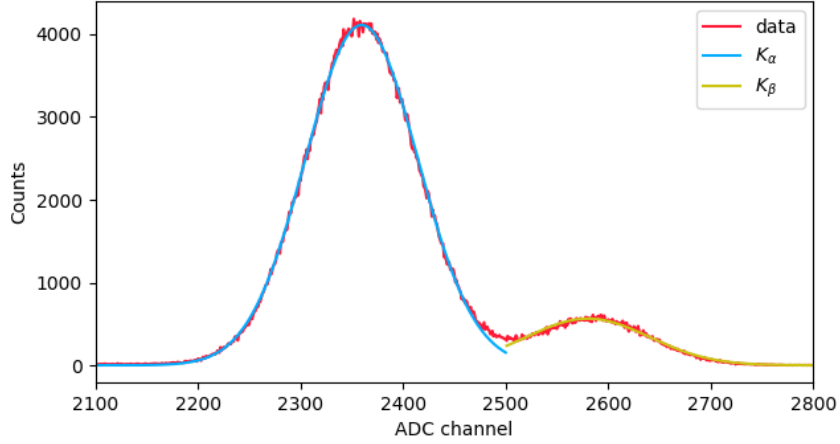


Figure A.2: Fe^{55} decay spectrum for a peaking time value of 8000 ns. Fit of the $\text{Mn-}K_{\alpha}$ and $\text{Mn-}K_{\beta}$ peaks. Clearly, the resolution is much worse than for a peaking time value of 800 ns.

A.2 Third chapter appendix

The error-bars of the FWHM of the photon and electron peaks in section 3.4.1 were both calculated using the standard deviation value of the fitted Gaussian functions as well as the errors linked to the calibration of the analog-digital-converter (ADC) scale.

$$\Delta FWHM = \sqrt{(\Delta\sigma \cdot m)^2 + (\Delta m \cdot \sigma)^2 + (\Delta y_0) - (2 \cdot \sigma_m \sigma_{y_0} \cdot \sigma)} \quad (\text{A.1})$$

Figure A.3 illustrates the procedure applied to determine the FWHM of the conversion electron peaks in section 3.4.1.

The energy calibration of each pixel has to be done separately, since the peak positions on the ADC-scale are shifted from pixel to pixel. The resulting curves are presented in A.4. The particular slope and offset values were plotted in figure A.5.

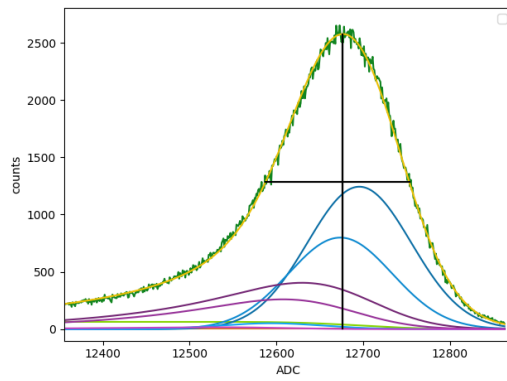


Figure A.3: Black horizontal line represents the FWHM of the L-32 conversion electron peak

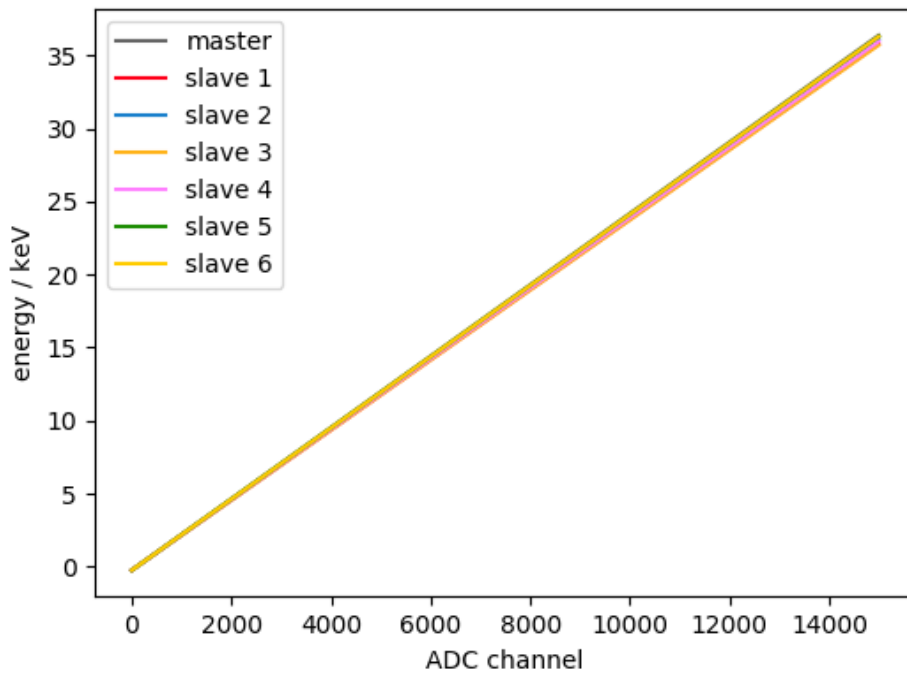


Figure A.4: Calibration curves of all pixels.

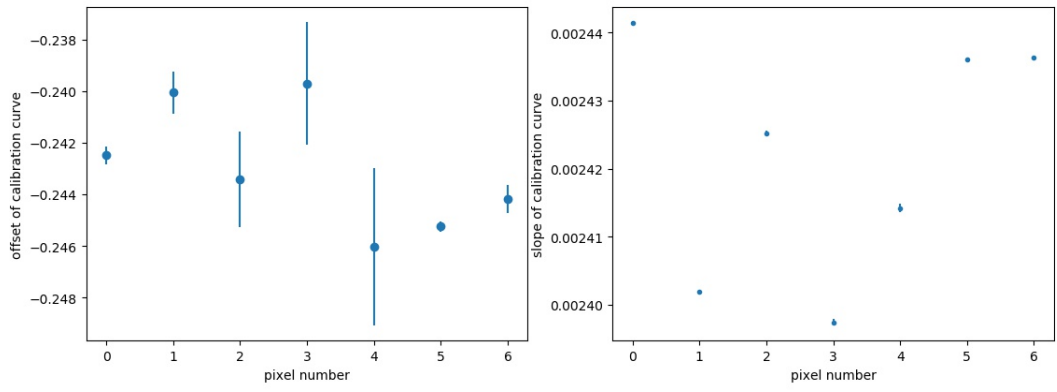


Figure A.5: Offset and slope of calibration curve, different pixels.

Bibliography

- [1] P. J. E. Peebles. »Dark matter«. In: *Proceedings of the National Academy of Science* 112 (Oct. 2015), pp. 12246–12248. DOI: 10.1073/pnas.1308786111. arXiv: 1305.6859.
- [2] A. Boyarsky et al. »Sterile Neutrino Dark Matter«. In: *ArXiv e-prints* (July 2018). arXiv: 1807.07938 [hep-ph].
- [3] Zykure. URL: https://commons.wikimedia.org/wiki/File:KATRIN_Spectrum.svg (visited on 05/09/2018).
- [4] The Katrin Collaboration. *KATRIN design report, FZKA Scientific Report 7090*. Tech. rep. Forschungszentrum Karlsruhe in der Helmholtz-Gesellschaft, 2005. URL: <http://bibliothek.fzk.de/zb/berichte/FZKA7090.pdf>.
- [5] The Health Physics Society. *Tritium*. 2011. URL: https://hps.org/documents/tritium_fact_sheet.pdf (visited on 07/2018).
- [6] E.W. Otten. »The Mainz neutrino mass experiment«. In: *Progress in Particle and Nuclear Physics* 32 (1994), pp. 153–171. ISSN: 0146-6410. DOI: [https://doi.org/10.1016/0146-6410\(94\)90016-7](https://doi.org/10.1016/0146-6410(94)90016-7). URL: <http://www.sciencedirect.com/science/article/pii/0146641094900167>.
- [7] V. N. Aseev et al. »Upper limit on the electron antineutrino mass from the Troitsk experiment«. In: 84.11, 112003 (Dec. 2011), p. 112003. DOI: 10.1103/PhysRevD.84.112003. arXiv: 1108.5034 [hep-ex].
- [8] Florian Heizmann, Hendrik Seitz-Moskaliuk and KATRIN collaboration. »The Windowless Gaseous Tritium Source (WGTS) of the KATRIN experiment«. In: *Journal of Physics: Conference Series* 888.1 (2017), p. 012071. URL: <http://stacks.iop.org/1742-6596/888/i=1/a=012071>.
- [9] Ellen Förstner. »Optimization of the KATRIN rear wall for a keV-scale sterile neutrino search«. Bachelor’s Thesis. Karlsruhe Institute of Technology, 2017.
- [10] G Beamson, H Q Porter and D W Turner. »The collimating and magnifying properties of a superconducting field photoelectron spectrometer«. In: *Journal of Physics E: Scientific Instruments* 13.1 (1980), p. 64. URL: <http://stacks.iop.org/0022-3735/13/i=1/a=018>.

- [11] J. F. Amsbaugh et al. »Focal-plane detector system for the KATRIN experiment«. In: *Nucl. Instrum. Meth.* A778 (2015), pp. 40–60. DOI: 10.1016/j.nima.2014.12.116. arXiv: 1404.2925 [physics.ins-det].
- [12] R. Adhikari et al. »A White Paper on keV sterile neutrino Dark Matter«. In: 1, 025 (Jan. 2017), p. 025. DOI: 10.1088/1475-7516/2017/01/025. arXiv: 1602.04816 [hep-ph].
- [13] Susanne Mertens. *Astroparticle Physics Lecture*. Feb. 2017.
- [14] G. B. Gelmini, E. Osoba and S. Palomares-Ruiz. »Inert-sterile neutrino: Cold or warm dark matter candidate«. In: 81.6, 063529 (Mar. 2010), p. 063529. DOI: 10.1103/PhysRevD.81.063529. arXiv: 0912.2478 [hep-ph].
- [15] Tim Brunst et al. »Detector Development for a Sterile Neutrino Search with the KATRIN Experiment«. In: *7th International Pontecorvo Neutrino Physics School Prague, Czech Republic, August 20-September 1, 2017*. 2018. arXiv: 1801.08182 [physics.ins-det].
- [16] S. Mertens et al. »Sensitivity of next-generation tritium beta-decay experiments for keV-scale sterile neutrinos«. In: *Journal of Cosmology and Astroparticle Physics* 2015.02 (2015), p. 020. URL: <http://stacks.iop.org/1475-7516/2015/i=02/a=020>.
- [17] Material accessible internally belonging to the KATRIN/TRISTAN group led by S. Mertens at the Max Planck Physics Institute.
- [18] S. Mertens et al. »Wavelet approach to search for sterile neutrinos in tritium β -decay spectra«. In: *Phys. Rev. D* 91 (4 Feb. 2015), p. 042005. DOI: 10.1103/PhysRevD.91.042005. URL: <https://link.aps.org/doi/10.1103/PhysRevD.91.042005>.
- [19] Tobias Bode et al. »Characterization of a prototype silicon drift detector system for the TRISTAN project«. In: (2018). not yet published, but accessible internally to the KATRIN/TRISTAN group led by S. Mertens at the Max Planck Physics Institute.
- [20] F. Perotti and C. Fiorini. »Observed energy dependence of Fano factor in silicon at hard X-ray energies«. In: *Nuclear Instruments and Methods in Physics Research A* 423 (Mar. 1999), pp. 356–363. DOI: 10.1016/S0168-9002(98)01264-9.
- [21] Thermo Fisher Scientific – Materials & Structural Analysis. *An Introduction to Silicon Drift Detectors*. 2015. URL: <https://www.azom.com/article.aspx?ArticleID=11973> (visited on 08/2018).
- [22] Jonathan Finley. *Physics of Nanostructured Materials*. 2018. (Visited on 08/2018).

- [23] L. Strüder and B. Titze. *PNSensor - Research and Development of Advanced Radiation Detectors*. URL: <http://www.pnsensor.de/Welcome/Detectors/SDD/index.php> (visited on 08/2018).
- [24] Tobias Eggert. »Die spektrale Antwort von Silizium-Röntgendetektoren«. Dissertation. München: Technische Universität München, 2004.
- [25] Halbleiterlabor of the Max-Planck-Society. URL: <https://www.hll.mpg.de/> (visited on 10/09/2018).
- [26] XGLab Bruker Nano Analytics Division. URL: <https://www.xglab.it/> (visited on 08/2018).
- [27] Laboratoire National Henri Becquerel. *Table de Radionucléides*. 2006. URL: http://www.nucleide.org/DDEP_WG/Nuclides/Fe-55_tables.pdf (visited on 08/2018).
- [28] Soo Hyun Byun. *Radiation & Radioisotope Methodology*. URL: https://www.science.mcmaster.ca/radgrad/images/6R06CourseResources/4RA34RB3_Lecture_Note_6_Pulse-Processing.pdf (visited on 08/2018).
- [29] AMETEK. *Understanding energy resolution*. URL: <http://atomfizika.elte.hu/muszerek/Amptek/Documentation/Application%20Notes%20and%20FAQs/Understanding%20energy%20resolution.pdf> (visited on 08/2018).
- [30] XGLab S.R.L. *User manual of DANTE Digital Pulse Processor*. 2018.
- [31] D. Venos et al. »Long term stability of the energy of conversion electrons emitted from solid $^{83}\text{Rb}/^{83\text{m}}\text{Kr}$ source«. In: *ArXiv e-prints* (Feb. 2009). arXiv: 0902.0291 [physics.ins-det].
- [32] D. Vénos et al. »Properties of $^{83\text{m}}\text{Kr}$ conversion electrons and their use in the KATRIN experiment«. In: *Journal of Instrumentation* 13.02 (2018), T02012.
- [33] Ostrick Beatrix. »Eine kondensierte $^{83\text{m}}\text{Kr}$ -Kalibrationsquelle für das KATRIN Experiment«. PhD thesis. Karlsruhe Institute of Technology, 2008.
- [34] Moritz Machatschek. »Simulation of the $^{83\text{m}}\text{Kr}$ Mode of the Tritium Source of the KATRIN Experiment«. MA thesis. Karlsruhe Institute of Technology, 2016.
- [35] *Internal Conversion*. URL: http://www.radioactivity.eu.com/site/pages/Internal_Conversion.htm (visited on 08/2018).
- [36] Egon Bücheler Peter Thurn. *Einführung in die radiologische Diagnostik*. Thieme, Stuttgart, 1998.
- [37] A. D. McNaught and A. Wilkinson. *IUPAC. Compendium of Chemical Terminology, 2nd ed. (the "Gold Book")*. Blackwell Scientific Publications, Oxford, 1997.

- [38] Hardouin Duparc, Olivier. »Pierre Auger et Lise Meitner : Comparaison de leurs contributions à l'effet Auger«. In: *Reflets phys.* 18 (2010), pp. 23–25. DOI: 10.1051/refdp/2010006. URL: <https://doi.org/10.1051/refdp/2010006>.
- [39] Till Stensitzki Matthew Newville. *Python's lmfit package*. URL: <https://lmfit.github.io/lmfit-py/> (visited on 05/2018).
- [40] B. L. Wall et al. »Dead layer on silicon p-i-n diode charged-particle detectors«. In: *Nuclear Instruments and Methods in Physics Research. Section A, Accelerators, Spectrometers, Detectors and Associated Equipment*, 744:73-79 (Apr. 2014). DOI: 10.1016/j.nima.2013.12.048.
- [41] J.C. Ashley and V.E. Anderson. »Interaction of low-energy electrons with silicon dioxide«. In: *Journal of Electron Spectroscopy and Related Phenomena* 24.2 (1981), pp. 127–148. ISSN: 0368-2048. DOI: [https://doi.org/10.1016/0368-2048\(81\)80001-1](https://doi.org/10.1016/0368-2048(81)80001-1). URL: <http://www.sciencedirect.com/science/article/pii/0368204881800011>.
- [42] Torsten Armbrust. »Messung der Eigenschaften eines Silizium Drift Detektors mit Elektronen im keV-Bereich«. MA thesis. Karlsruhe Institute of Technology, 2004.